Optical diagnosis on dusty plasmas for nanocrystalline thin film silicon solar cells

Master thesis by Casper van der Wel
Supervisor: Akshatha Mohan MSc
Dr. Jatin Rath

Nanophotonics - Physics of Devices, Debye Institute for Nanomaterials Science,
Utrecht University, P.O. Box 80000, 3508 TA Utrecht, The Netherlands

(Dated: 01 December 2012)

Abstract

Thin film solar cells from hydrogenated silicon are viable solutions for mass production of electricity from solar energy. In the production of solar cells with plasma enhanced chemical vapour deposition (PECVD), the well-known effect of gas phase nucleation of silicon quantum dots can lead to the incorporation of nanocrystals resulting in improved optoelectronic properties. In this thesis, a stable and reproducible fluctuation of 10-50 Hz in emission and current was observed in dusty hydrogen-diluted silane plasmas. It was concluded that this fluctuation originates from the plasma dynamics caused by the growing dust particles. In the development of a new plasma reactor, also a substrate temperature calibration was done, in which was found that the substrate temperature is not only dependent on the heater temperature, but also on the substrate holder and the gas pressure. Finally, a setup for scattering experiments on dust particles (LLS) was developed and tested. With the setup using 90° scattering, a dust scattered signal was detected. A literature study on dusty plasmas is included in this thesis to provide a background for the continuation of the research project in the new reactor.

Table of contents

Introduction

With a growth rate of 40% per year [1], the global photovoltaic market is one of the fastest growing markets in the world. While crystalline solar cells still are the main source of solar energy conversion, thin film solar cells from amorphous hydrogenated silicon also form a significant part (5-10% [2]). Thin film solar cells have advantages in their material and production costs [3], however their efficiency is lower than the crystalline counterparts. Recent developments in 50 μm thin crystalline silicon wafers [4] and other thin film materials such as CdTe and $CuInS_2$ are becoming major competitors for the advantages of thin film solar cells.

A fundamental new area for the increase of the efficiency of thin film solar cells is the incorporation of plasma synthesized quantum dots [5]. In the production of solar cells with the conventional plasma enhanced chemical vapour deposition (PECVD), silane molecules can polymerize into clusters. The particles acquire a net negative charge and are therefore trapped by the plasma potential profile [6]. At a certain concentration, the silicon clusters start to aggregate into larger agglomerates: the plasma dust, which eventually is expelled from the plasma by ion drag, gravity and/or thermophoretic forces.

This well-known effect of dust formation has already been subject to research since the early 90s, because it leads to impurities and short-circuiting in the deposited layers. It has recently been shown that the incorporation quantum dots (which are the dust precursors) in a silicon layer can result in improved optical and electronic properties [7–9]. In order to control the plasma synthesis and deposition of quantum dots, a new plasma chamber has been developed in the Physics of Devices group, which will be able to extract quantum dots from the plasma with a temperature gradient.

This thesis includes two parts: first the literature study on dusty plasmas provides a broad background for the continuation of this research. The described experiments are initial studies on the dusty plasmas and experimental set-ups that will be used in the new chamber. In order to control the nucleation and growth of silicon particles, the (dusty) γ' regime has to be understood on a fundamental level. The γ' regime has been studied optically, with an optical emission spectrometer (OES) and a photomultiplier tube (PMT), and electrically, with a built-in VI-probe. Next to these plasma studies, the influence of several parameters on the substrate temperature was investigated and a scattering (LLS) setup was developed.

Chapter 1   Literature study

In this section a theoretical framework for dusty silane deposition plasmas is drawn up. This literature study will be focussed especially on nanoparticles in size range of 1-10 nm. The term 'dust' will be used as a general term for all clusters, aggregates and powders in the range of 1 nm – 1 μm.

Dusty plasmas have been subject to research from the early 90s. The more fundamental research of the first decade was summarized by several experts in 1999 in *Dusty Plasmas, Physics, Chemistry and Technological Impacts in Plasma Processing* [10–13], on which this chapter is largely based. Recent developments are mainly based on recent review articles by Shukla and Eliasson [6], Fortov et al. [14], and Ostrikov et al. [15].

The structure of this chapter is shown in the table of contents below. In the first two sections, the general physics and chemistry of silane dusty plasmas will be introduced. The third section will cover the dynamics of the dusty plasma, which is important for both dust synthesis and deposition. In the fourth section, several *in situ* plasma diagnostics will be described, focussed on the detection of quantum dots.

TABLE OF CONTENTS

1.1 SILANE PLASMAS IN PECVD

A widely used technique for thin-film (1 nm – 1 µm thickness) silicon deposition is plasma enhanced chemical vapour deposition. In PECVD, a plasma is created by a radio frequency (1-100 MHz) potential between two parallel electrodes. The ions and radicals produced in the plasma form a layer on the substrate that is usually mounted on the top electrode, which is usually grounded. The nature of the deposited layer is determined by the conditions of the deposition plasma, which will be described in this section.

1.1.1 General plasma physics

A plasma consists of a gas with ions (charged gas particles) and electrons. Positive particles induce a cloud of negative particles around themselves, so that the electric field decays more rapidly than in vacuum. The characteristic length of this extra exponential decay factor is called the *Debye length*, which depends on the 'charge shielding ability' of the plasma: the charge, density and temperature of all charged species:

Debye length
$$\lambda_D = \sqrt{\frac{\varepsilon_0 k_B T}{\sum_j q_j^2 n_j}} \approx \sqrt{\frac{\varepsilon_0 k_B T_e}{q^2 n_e}}$$
1

The electron temperature is denoted by T_e and electron density by n_e. The constants ε_0, q, and k_B denote the vacuum permittivity, the elementary charge, and the Boltzmann constant, respectively. In a PECVD plasma, the electron mobility is very high in comparison with the ion mobility and therefore the total shielding is approximately equal to the electron shielding. At common high frequency PECVD conditions of $T_e = 3$ eV and $n_e = 10^{15}$ m^{-3}, the Debye length is a few tenths of millimetres [16,17].

Due to the enormous electrostatic restoring force, a local excess of charge is immediately neutralized at length scales larger than the Debye length. This *quasi-neutrality* condition results in zero electric field and a constant potential inside the plasma. It is called *quasi* because it is only valid at length scales larger than λ_D. Also due to this electrostatic restoring force, particles fluctuate around neutrality with a frequency that is called the *plasma frequency*. This frequency depends on the particle inertia and it defines the smallest timescale in the plasma [16]:

Plasma frequency for electrons
$$\omega_{p,e} = \sqrt{\frac{n_e q^2}{m_e \varepsilon_0}}$$
2

The plasma frequency of electrons $\omega_{p,e}$ is an angular frequency which is related to the ordinary frequency via $\omega = 2\pi f$. m_e denotes the electron mass, which is much lower than the ion mass, so that electrons are a faster species: typical values for the plasma frequency are 1 GHz for electrons and 10 MHz for ions. Because of these timescales, electrons can easily follow the 10-100 MHz electric field used in PECVD, but ions are too slow and only react on the averaged field.

1.1.2   Electrical aspects of a PECVD plasma

An RF PECVD plasma is formed between two electrodes with an applied RF potential, which is in our case capacitively coupled so that no net (DC) current can flow. Free electrons are accelerated and gain enough energy to ionize gas atoms, producing more electrons and creating an electron avalanche that sustains a discharge between the electrodes. The discharge occurs at a certain breakdown voltage between the electrodes, which is determined mainly by the product of pressure and electrode distance: the *pd-product*. When the electron mean free path is large (low pressure) and the electrode distance small, the electrons have less chance to ionize gas atoms and create an avalanche. On the other hand, when the electron mean free path is low (high pressure) and the electrode distance large, the electrons lose too much energy due to inelastic collisions. Therefore, the breakdown voltage is lowest at an optimum value of *pd*. This effect is described by the Paschen curve (Figure 1).
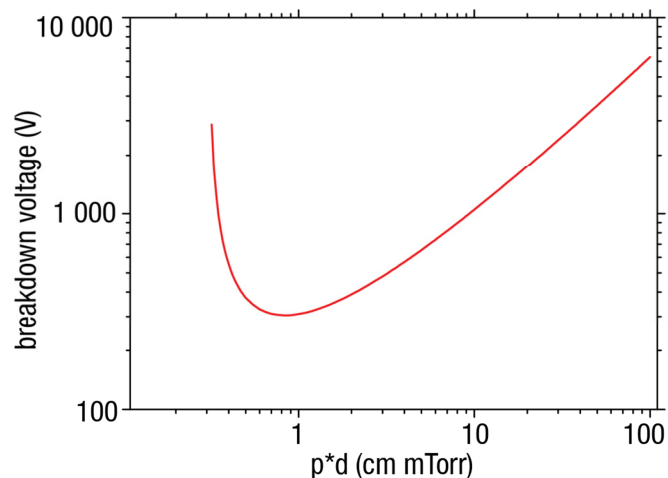
Figure 1: Paschen curve for the breakdown of air; 1 mTorr equals 1.33 mbar. Picture source: [18]

There are several discharge types. In the glow discharge, the free charge carrier density is large and a neutral plasma bulk is formed by Debye shielding. The Debye length is comparable or smaller than the interelectrode distance. Sheaths are formed at the plasma sides where the space charged is concentrated.

When a plasma is used for deposition, the electrodes are often quickly covered by an insulating layer. This would give problems for sustaining a direct current (DC) discharge, which can be overcome by applying an alternating (AC) potential. This is done in PECVD: a plasma is sustained between two electrodes at an AC potential oscillating at radio-frequency (10-100 MHz) speed.

1.1.3   The plasma sheath

Due to the quasi-neutrality, a neutral plasma bulk is created, with a constant potential and no electric field. The alternating potential difference occurs in the regions between the plasma bulk and electrodes: the *sheath* regions. These regions shield the plasma bulk from the electrodes and have a thickness of tens (10-40) of Debye lengths [18].

The ion dynamics and resulting potential profile of a flat electrode can be derived from the assumption that at plasma equilibrium, electrons follow the Maxwell-Boltzmann distribution. This assumption is justified as all dynamics are much slower than the electron characteristic timescale of $\approx 10^{-9}$ s. If we also assume no ionization

inside the sheath, we can use an equation of constant ion flux to the electrodes. These assumptions, together with energy conservation, lead to the following equations:

Electron distribution
$$n_e(x) = n_{e,s}e^{\frac{-qV(x)}{kT_e}}$$
3

Constant ion flux
$$\Gamma_{ion} = n_{i,s}v_{i,s} = n_i(x)v(x)$$
4

Ion energy conservation
$$\frac{1}{2}m_iv_{i,s}{}^2 = \frac{1}{2}m_iv_i(x)^2 + qV(x)$$
5

A subscript s denotes the sheath edge and the distance x is the distance from the sheath edge towards the electrode. $V(x)$ is the local potential with respect to the sheath edge, Γ_{ion} denotes the ion flux, n_e and n_i the electron and ion densities, m_i the ion mass, v_i the average ion speed, k the Boltzmann constant and q the elementary charge.

With these equations, the total charge density $\rho(x)$ can be expressed in the local potential $V(x)$. Assuming only singly ionized species, which is a good assumption in RF plasmas, the charge density in the sheath is as follows:

Charge density
$$\rho(x) = \frac{qn_{i,s}v_{i,s}}{\sqrt{v_{i,s}{}^2 - 2qV(x)/m_i}} - qn_{e,s}e^{\frac{-qV(x)}{kT_e}}$$
6

Now the potential can be solved using the Poisson equation [10]. This equation only has a real solution when $m_iv_{i,s}^2 > kT_e$. This sets a minimum ion velocity at sheath entrance, which is called the *Bohm velocity* or *Bohm criterion*. As the ions in a PECVD plasma have a much lower thermal velocity, this criterion can only be reached if there is a region in which the ions are accelerated. This region is called the *pre-sheath* and the minimal potential difference between plasma bulk and pre-sheath is as follows (using equation 5):

Pre-sheath potential
$$q(V_s - V_p) = \frac{1}{2}kT_e$$
7

V_p denotes the plasma bulk potential and V_s the potential at the sheath boundary. With this potential difference, the electron density at the sheath boundary can be expressed in the plasma bulk electron density (from equation 3): $n_{e,s} = e^{-0.5}n_e \approx 0.6\,n_e$. As the pre-sheath region is a neutral region, the ion density is the same and the ion flux can be calculated from the Bohm velocity:

Bohm flux
$$\Gamma_{Bohm} = e^{-0.5}n_e\sqrt{\frac{kT_e}{m_i}}$$
8

Independent on the electrode potential, this Bohm flux is always pointing out of the plasma. The plasma bulk is therefore always at a higher potential than the electrodes. By this potential, positive ions are accelerated outwards and negative species are contained within the plasma. The electron flux to the electrodes is derived from integration of a Maxwell-Boltzmann velocity distribution of electrons, giving the electron flux dependence on the potential difference between electrode and plasma sheath edge. Using equation 7 this can be related to the plasma bulk potential: $V_e - V_s = (V_e - V_p) + \frac{1}{2q}kT_e$. This gives the following electron flux:

Electron flux
$$\Gamma_e = \frac{e^{-0.5} n_e}{4} \sqrt{\frac{8kT_e}{\pi m_e}} e^{\frac{q(V_e - V_p)}{kT_e} + \frac{1}{2}}$$
9

Flux equations 8 and 9 can be used to obtain an equation for the current through the electrodes. Furthermore, the equations for planar sheaths are also valid for large isolated objects inside the plasma. By equating the two fluxes, the following *floating potential* can be derived for an isolated large (dimensions $\gg \lambda_D$) object. By convention, this potential is given with respect to the plasma bulk potential V_p.

Floating potential
$$V_f = -\frac{kT_e}{2e}\left[1 + \ln\frac{m_i}{2\pi m_e}\right]$$
10

In the PECVD setups described in this thesis, the powered electrode is coupled to the power source via a capacitor. In this way, there can be no net current through the plasma: the current averaged over one potential cycle is zero. Also, from Kirchhoff's law it follows that the current through both electrodes must be equal. As the powered electrode is floating, it can develop a constant (DC) potential: $\Delta V(t) = V_0 \sin \omega t + V_{DC}$. From the flux equations and above relations, the electrode potentials and a constant bias potential can be solved numerically. The resulting potential profile is shown schematically in Figure 2 and Figure 3. In Figure 3, a minor effect of the displacement current associated with the charging of the plasma sheath is also included [18].
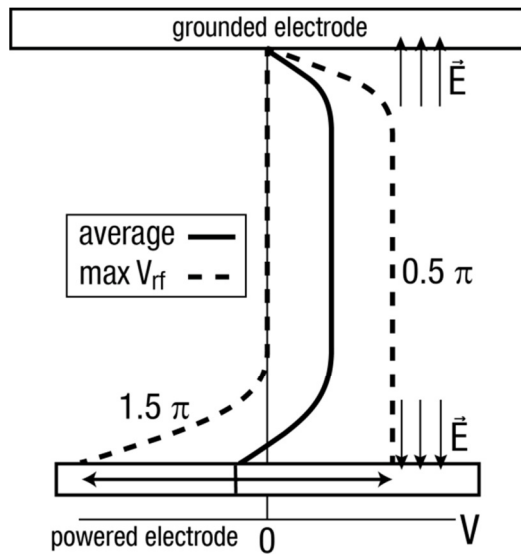
Figure 2: Plasma potential profile in PECVD. The average and the two extrema at $\phi = 0.5\ \pi$ and $1.5\ \pi$ are shown.
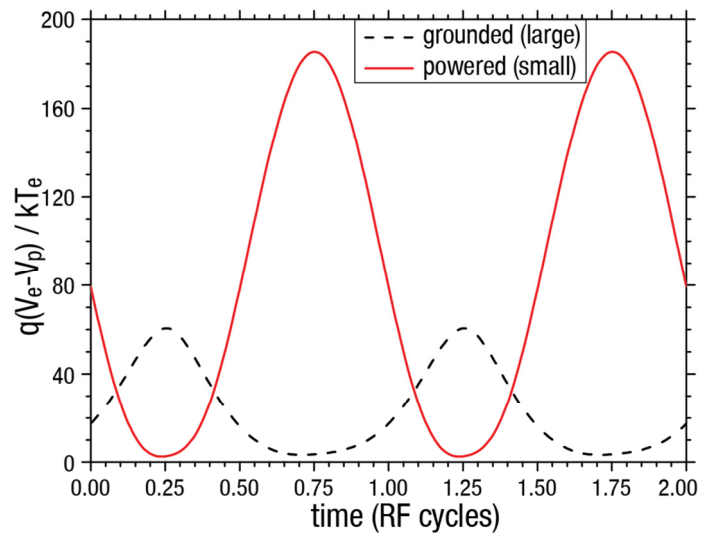
Figure 3: Time development of the electrode potentials (with respect to the plasma potential). Picture source: [18]

The *bias voltage* V_{DC} is a result of the reactor asymmetry: the grounded electrode consists of the reactor wall and the grounded electrode and is far larger than the powered electrode, so that a lower potential difference is necessary at the grounded electrode to reach the same current.

Positive ions cannot react to the RF field and feel the averaged potential, so that they can only be accelerated in the sheath towards the electrodes. Negative ions are contained inside the plasma bulk by this potential. Due to the bias voltage, the ion bombardment at the powered electrode is more severe, so that the substrate for film deposition is normally mounted on the grounded electrode.

1.1.4 Gas dynamics

The average gas residence time τ at steady state conditions is given by the number of particles inside the reactor N_R divided by the number of particles flowing in per second Q. The gas inflow S is measured in sccm (cm^3 per minute at standard atmospheric temperature and pressure). The reactor pressure is so low that the ideal gas law is a good approximation. Using the reactor volume V_R, the average particle residence time can be calculated using the following equation, in which p, T and R are the pressure, temperature, and gas constant, respectively. The subscript 0 denotes standard atmospheric conditions ($p = 100$ kPa and $T = 0$ °C).

$$\tau = N_R/Q = \frac{pV_R}{RT}\bigg/\frac{p_0 S}{RT_0} = \frac{V_R(p/p_0)}{S(T/T_0)} \qquad\qquad 11$$

The gas dynamics in the initial phase of the plasma differ from the rest of the plasma time. This different gas composition during this transient behaviour gives rise to an *incubation layer* of different morphology [19]. The thickness of this layer is dependent on the plasma equilibration time, which is of the order of the average gas residence time [20]. During this time, a steady state is established inside the plasma. This process is slowed by s*ilane back diffusion*. For laboratory reactors, there is relatively much 'inactive' space around the plasma: in this space, silane does not react. When the plasma is created, silane diffuses into the reactive region until silane concentration in both regions is equal. Due to this effect, silane concentration is higher during the initial transient and this has important consequences for the incubation layer [21].

1.1.5 Chemical properties

The gas phase chemistry of a silane-hydrogen (SiH_4:H_2) discharge is described by a large set of mutually influencing reactions. They can be distinguished into categories: primary reactions, radical-molecule reactions, ion-molecule reactions and radical-radical reactions [22]. This subsection will give a short overview of the most important reactions.

Primary reactions take place by electron impact dissociation of silane and hydrogen molecules. In this way positive species (SiH_n^+, H_2^+), negative species (SiH_n^-) and radicals ($SiH_n\cdot$, $H\cdot$) are produced [23]. Polysilyl species (especially disilyl and trisilyl) formed through secondary reactions also undergo electron impact dissociation. The radicals (especially $SiH_3\cdot$) are the main precursors for the silicon layer growth [22,24]. In conventional RF PECVD, branching ratios for the silane dissociation at an electron energy of 70 eV are applicable: $SiH_3\cdot$ / $SiH_2\cdot$ / $SiH\cdot$ / $Si\cdot$ are produced in the ratios 43% / 36% / 12% / 9% [23]. These ratios however depend strongly on the average electron energy, which in the case of VHF (very high frequency) PECVD usually is much lower (3-10 eV). The primary reactions of silane and hydrogen are summarized in equations 12 to 15.

$$SiH_4 + e^- \rightarrow SiH_3 \cdot / SiH_2 \cdot / SiH \cdot / Si \cdot + (H \text{ products}) + e^- \quad \text{(electron impact dissociation)} \quad 12$$

$$H_2 + e^- \rightarrow 2H \cdot + e^- \quad \text{(electron impact dissociation)} \quad 13$$

$$SiH_4 + e^- \rightarrow SiH_3^+ / SiH_2^+ / SiH^+ / Si^+ + (H \text{ products}) + 2\,e^- \quad \text{(ionization)} \quad 14$$

$$SiH_4 + e^- \rightarrow SiH_3^- / SiH_2^- / SiH^- + (H \text{ products}) \quad \text{(electron attachment)} \quad 15$$

$$SiH_4 + H \cdot \rightarrow SiH_3 \cdot + H_2 \quad \text{(hydrogen abstraction)} \quad 16$$

$$SiH_n \cdot + e^- \rightarrow SiH_n^- \quad \text{(secondary electron attachment)} \quad 17$$

$$Si_nH_m^- + SiH_4 \rightarrow Si_{n+1}H_{m'}^- + (H \text{ products}) \quad \text{(anion-molecule clustering)} \quad 18$$

$$Si_nH_m + SiH_4 \rightarrow Si_{n+1}H_{m'} + (H \text{ products}) \quad \text{(radical-molecule clustering)} \quad 19$$

In normal a-Si depositions, the degree of silane dissociation is around 10% [24], but at high electron densities, silane dissociation efficiency increases so that its concentration in the plasma zone becomes low. This effect is called the *silane depletion*. Because the silane depletion factor is an important parameter for the structure of the deposited layer and the rate of the deposition, it has been subject to much research [3,25]. At high depletion conditions, secondary reactions become dominant.

The presence of atomic hydrogen in the gas phase creates another pathway for the creation of silyl radicals: the *hydrogen abstraction* reaction (equation 16) [3]. This reaction also occurs with polysilyl species and contributes to the depletion of silane gas. Because of the large silane depletion, the electrons react with secondary species: there are many silyl anions formed by secondary electron attachment (equation 17) [26]. These negative species are the principal precursors for silicon cluster growth via the reaction in equation 18, as their residence time in the plasma zone is large. A nucleation route with radical-molecule reactions also exists (equation 19), starting from neutral silyl precursors. The polysilyl species become charged later by electron attachment [11]. However, the dust nucleation is governed mostly by negative species [26–28]. An important notion is that dust formation is faster in 'dusty' reaction chambers: previous dust precursors may be sputtered from the wall enhancing the dust concentration [29].

1.2 DUSTY PLASMAS

1.2.1 Silicon dust formation

The formation of plasma dust is, in general, a sequence of four steps [11]. After the nucleation phase where clusters of 100-1000 atoms are formed, there is a period of charging and growth of particles. At a certain critical size of 3-10 nm and density of 10^{16}-10^{18} m^{-3}, these particles start to feel each other and aggregate into isolated multiply-charged aggregates of 10-100 nm. Finally their growth continues by deposition, with a rate similar to thin film deposition. See Figure 4 for a schematic overview of the dust formation.
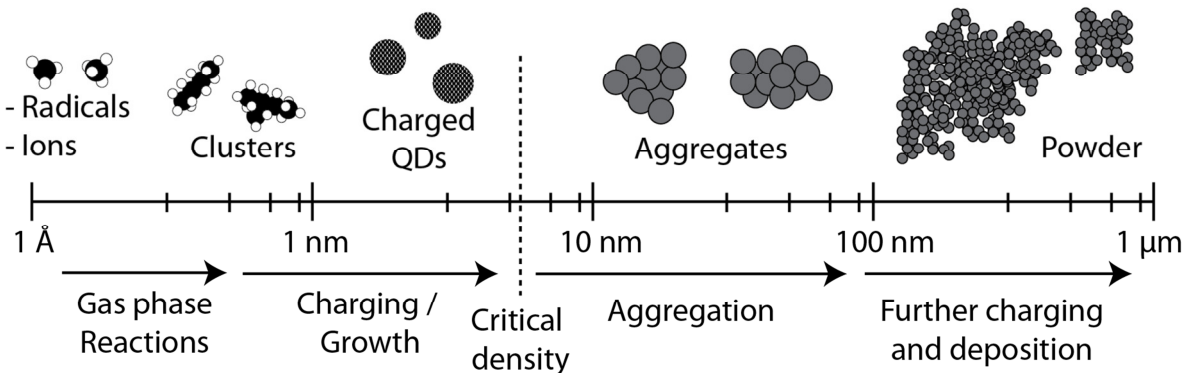
Figure 4: Growth steps in the formation of nanoparticles in a silane PECVD plasma

The nucleation phase, as described in the previous section, results in silicon clusters of 100-1000 Si particles with sizes between 2 and 4 nm. As the electron temperature is much higher than the ion temperature, the particles become negatively charged (see section 1.2.3) and are suspended inside the plasma due to the electric fields in the sheaths. The large amount of particles however also influences the plasma due to extra electron attachment: electron density decreases. It has been observed that the average particle charge in this stage is normally below unity, making deposition of quantum dots possible [11,30]. The characteristics of the dusty plasma and the charging of the quantum dots will be examined more closely in sections 1.2.2 and 1.2.3.

When the nanoparticles reach a critical density their interaction energy becomes important (section 1.2.5) and at a certain critical density, particle growth proceeds via aggregation. For this effect, the plasma can be considered as a solid/plasma colloid, similar to solid/gas colloids (aerosols). These colloids are thermodynamically unstable: they aggregate. A relatively simple aggregation model is the Brownian free molecular coagulation model (BFMC). Despite that this model describes coagulation of neutral particles, the model describes the start of aggregation rather accurately, because of the small and strongly fluctuating charge on the quantum dots [30]. Further into the aggregation phase, the particles become more charged and the model starts to deviate. This aggregation increases the particle radius quickly from several nm to 50-100 nm with charges of the order of 10-3000 elemental charges (proportional to the dust radius [10]).

After the aggregation phase, the particles grow with a rate close to the growth rate corresponding to the deposition rate [11]. The balance between ion flux and electron flux results in a strong negative charge (see section 1.2.3). They are trapped inside the plasma and can grow to several micrometres.

The forces acting on silicon clusters and dust particles are further described in section 1.2.4.

1.2.2   The α-γ' transition

The dust particles in a plasma have a strong influence on the plasma parameters. When the dust agglomerates, a clear transition takes place between the so-called α and γ' regimes [31]. During the transition, the electron density decreases and the electron temperature increases. Debye shielding is less effective, the sheaths become broader, and ionization and deposition rates increase.

The transition can be explained via the charge neutrality inside the plasma bulk: as the dust particles become more negative, the electron density has to decrease to maintain the quasi-neutrality condition (equation 20). The effect of this electron depletion is described by the *Havnes parameter* $P = Z_D n_D / n_e$, in which Z_D denotes the dimensionless dust charge and n_D the density of dust particles.

Quasi-neutrality $$n_i = n_e + Z_D n_D = (1 + P)n_e \qquad\qquad 20$$

As the power applied to the plasma is kept constant, the electron temperature increases. The dust particles collect a constant flux of ions and electrons (section 1.2.3). To compensate for this extra loss, the rates of ion and electron production have to be increased; otherwise the discharge would cease. These rates are increased by increasing the electrode potential. With this increase, the electrons are accelerated to a higher temperature. As the electrons are the energy source of all primary reactions, the dissociation and ionization rates increase [32].

The increase of charged particle losses results in an increase of plasma resistance. In the α-regime, the resistance is low and the plasma is almost purely capacitive (the electrode potential lags the current by 85-90°). An increase of resistance results in a lower voltage-current phase shift, which can be measured directly [31,33].

The lower electron density and higher electron temperature directly result in an increase of the Debye length. Consequently the plasma sheaths become broader, which is clearly visible. Due to gravity, the dust cloud is suspended in the lower part of the plasma. These effects make the α-γ' transition directly observable by 'visual inspection' (see Figure 5). In this figure, the α-regime is asymmetric due to the reactor asymmetry [34], but the γ' regime even more due to the dust cloud. The emission can be analysed more quantitatively by spatially resolved optical emission spectroscopy [35].

Figure 5: Picture of a silane plasma in α-regime (left) and γ'-regime (right). Pictures source: [34]

The transition is induced by the dust agglomeration, in which the dust charge rapidly increases. Agglomeration can only be reached when the particles have enough time to reach the critical density before they are expelled from the plasma: the competition between initial particle growth time and silicon cluster residence time separates the α and γ' regimes. The γ' regime is favoured by high power, high pressure, low temperature, low

gas flow rate, and low silane dilution. Also the flow pattern is important: in a so-called 'showerhead' [33] design, the gas flows in through a grid on the bottom (powered) electrode, to ensure a vertical homogeneous gas flow. In such a design, dust is less easily blown to the sides and the γ' regime can be reached more easily than in a reactor with a gas inlet on the side. This aspect is closely related to the plasma dynamics, which are described in section 1.3.

1.2.3   Charge and potential of plasma dust

The electron flux, ion flux and floating potential of large plasma-immersed objects (dimensions $\gg \lambda_D$) have already been described in section 1.1.3. As the Debye length in silane plasmas is a few tenths of millimetres and increases with growing plasma dust, the dust is much smaller than λ_D and a different theory for the electrical description of plasma dust is required. This theory describes the motion of charged particles in a Debye-Hückel potential and is called the Orbit Motion Limited theory (OML). A short overview of his theory is given in this section; for a more thorough analysis and complete derivations see [10,14].

The potential around a charged dust particle of charge Z_D is described by the Debye-Hückel or Yukawa potential (equation 21). When both electrons and ions follow a Boltzmann distribution and the potential at any point in the plasma is much smaller than the electron and ion kinetic energies ($eV \ll kT_i$), the characteristic shielding length around the particle can be related to the ion and electron Debye lengths (equation 22). This *linearized Debye length* is closest to the ion Debye length, because of the lower ion energy in PECVD plasmas.

<table>
<tr><td>Debye-Hückel potential</td><td>$$V(r) = \frac{Z_D q}{4\pi \varepsilon_0 r} e^{-\frac{r}{\lambda_{DL}}}$$</td><td>21</td></tr>
<tr><td>Linearized Debye length</td><td>$$\frac{1}{\lambda_{DL}{}^2} = \frac{1}{\lambda_{D,e}{}^2} + \frac{1}{\lambda_{D,i}{}^2} = \frac{q^2}{\varepsilon_0}\left(\frac{n_e}{kT_e} + \frac{n_i}{2E_i}\right)$$</td><td>22</td></tr>
<tr><td>Coulomb radius for ions</td><td>$$R_{C,i} = \frac{Z_D}{8\pi n_i \lambda_{D,i}{}^2}$$</td><td>23</td></tr>
</table>

In these equations, r denotes the (radial) distance from the dust particle under consideration, Z_D the dimensionless dust charge, λ_{DL} the linearized Debye length, and E_i the (average) ion energy. It is important to pay attention to the approximations for these equations. At a certain proximity to the particle, the local potential becomes too high for the approximation $eV \ll kT_i$ and the linearization (equation 22) breaks down. This limiting distance is called the *Coulomb radius* (equation 23). The Coulomb radius is most often not negligible, so this assumption is rigorous in a non-equilibrium plasma. However this linearization appears to be very close to more elaborate theories [10]. This is because normally $R_{C,i} < \lambda_{DL}$, so that the solution of the Debye-Hückel potential (equation 21) within the Coulomb radius is close to the Coulomb potential in which the Debye length does not play a role.

Charging occurs via collisions with ions and electrons. The collision cross-section for such a Coulomb collision between a dust particle at a potential $V(R)$, where R is the dust radius, and an incoming particle of charge Q and kinetic energy E_{kin} is given by equation 24 [16]. The electron kinetic energy consists of its thermal energy and can be expressed as kT_e. The ion velocity is however greatly affected by the local electric field and consists of a thermal part and an electric field induced drift part. Because of this, the energy in the equation is expressed as E_{kin}. For small particles, the potential on the dust surface $V(R)$ is proportional to the dust charge (eq. 25).

Collision cross-section
$$\sigma_{OML} = \pi R^2 \left(1 - \frac{QV(R)}{E_{kin}}\right)$$
24

Dust charge and potential
$$qZ_D = 4\pi\varepsilon_0 R \left(1 + \frac{R}{\lambda_{DL}}\right)V(R) \approx 4\pi\varepsilon_0 R V(R)$$
25

From this cross-section, the total ion and electron currents can be solved by integration according to the appropriate ion and electron energy distribution functions. At steady state, the currents are equal and the particle charge can be solved from this numerically. A useable approximation for mono-energetic ions and Maxwell distributed electrons is given in equation 26 [10]. As $m_e \ll m_i$ and $T_e \gg T_i$, the square root is > 1. The electron depletion ratio n_e/n_i is given by the *Havnes parameter* and reduces the dust charge when there is a large dust charge or concentration (see section 1.2.2). As this is a secondary effect, the logarithm is positive and the charge negative. Note that the dust charge is proportional to the dust radius and not to its surface.

Dust charge (B is an empirical constant)
$$Z_D \cong -B \frac{4\pi\varepsilon_0 R k T_e}{q^2} \ln \frac{n_e}{n_i} \sqrt{\frac{m_i T_e}{m_e T_i}}$$
26

The OML theory holds for small dust size ($R \ll \lambda_D$) under the following assumptions:

- The dust is non-interacting: the dust density $n_D \ll \lambda_D^{-3}$. For the interacting case, see section 1.2.5.
- Ions carry only a single charge. This is normally the case for PECVD plasmas.
- There are only few ions in the non-linear part of the particle potential: $n_i < R_C^{-3}$.
- The electrons density follows the Boltzmann distribution.
- An extra energy barrier in the potential introduces extra ion trajectories so that the OML theory is not valid anymore. The Debye-Hückel potential can exhibit an extra barrier, nonetheless this effect is negligible for dust sizes $R \ll \lambda_D$ [10].
- There are no collisions during the approach of the ion to the dust particle: $\lambda_D \ll \ell_i$.

The assumption of ion non-collisionality can be easily violated in PECVD. When an ion collides with a neutral gas particle that is also present in the dust potential, it loses its kinetic energy and is trapped in the potential. Due to this effect, the ion current to the dust particle is enhanced and the dust charge becomes less negative. The collisionality is described by the ratio between the ion mean free path $\ell_i = (n_n \sigma)$ and the Debye length. Even when the Debye length is ten times smaller than the ion mean free path, collisions affect the dust charge [14,36].

Also secondary electron emission and ion sputtering influences the charge. The emission of secondary electrons can be induced by ion bombardment or by UV radiation; ion sputtering is the emission of ions due to collisions with energetic particles.

1.2.4   Forces on dust particles

The dynamics of dust inside a plasma are governed by the forces working on dust particles. There are several forces acting on a dust particle, of which the most relevant are the electrostatic force, the (neutral and ion) drag forces, the thermophoresis force, the interparticle forces, and the gravitational force. For a full review, see [6,10,14].

For a small particle in a homogeneous plasma, the *electrostatic force* is in very good approximation proportional to the dust charge which in turn is proportional to the dust radius (see section 1.2.3). In the sheath regions there exists a gradient of the Debye length. In this region there exists an extra *polarization* force which is always directed inwards. However, this force is much smaller than the electrostatic force when $R \ll \lambda_D$ [10]. The electric field is the strongest in the sheath regions, where it points outwards so that negative particles are contained.

The *ion drag force* is believed to establish the dust location and configuration inside a radio-frequency PECVD plasma. The force mechanism is more complicated because of the Coulomb interactions and perturbations of the Debye sphere around the dust particle. On top of that, the ion-generation and thus the ion flow pattern depends on the local dust concentration. This interplay between forces and dust location will be described in section 1.3. The ion drag force can be split in two parts: the Coulomb collision and the ion collection part. For the collection of thermal ions by small particles, OML theory can be used (section 1.2.3). For the collisions with ions, there are several theoretical approaches [14,37]. For the small particles under consideration, the limiting case of the linearized Debye length can be used. The ion drag force depends on the ion drift velocity $\vec{u}_I$ and ion average speed v_i. When the drift velocity is much larger than the thermal speed, the average speed has to be corrected [37]. The model of ion drag given in Table 1 neglects collisionality, which does can play an important role.

The *neutral drag force* arises from collisions (momentum transfer) of dust particles with molecules without charge. When the mean free path of the neutral particles is much larger than the dust radius, the neutral drag force can be derived from a kinetic theory of hard-sphere collisions. The neutral gas particles have a Maxwell distribution. When the relative velocities are low compared to the neutral thermal speed, an approximation can be made that is shown in Table 1. In this model, no adsorption/desorption mechanisms are incorporated, but this generally is a good assumption. In a showerhead reactor, the gas flow is directed upwards, so that a net upwards neutral drag force is expected. Due to the low flow rates, neutral drag mainly acts as a damping force with damping constant K_{D-n}.

The *thermophoresis* effect arises from a temperature gradient. When the temperature on one side of the dust particle is higher than the temperature on the other side, there is an imbalance in the momentum transfer by collisions and the particle is directed to the low temperature side. By cooling one of the electrodes, this force can be used to extract dust particles, as is intended in Chamber 5 of ASTER. The force depends on the thermal conductivity κ_T of the neutral gas atoms, which in turn depends on their thermal speed and collision cross-section ($\kappa_T \simeq 0.01 - 0.04 \text{ W K}^{-1}\text{m}^{-1}$ for gases).

The *gravitational force* is directed downwards and scales with the particle volume R^3. For small particles, this force is usually much smaller than the electrostatic and drag forces.

The sum of these forces determines the time-dependent arrangement of dust particles inside the plasma. A phenomenon that has been studied extensively in the last years is the formation of a dust-free *void* region inside the dust cloud [38,39]. This void is formed by a balance of the electrostatic forces suspending the particles in the plasma and ion drag force from ions accelerated out of the reactive plasma centre (see section 1.3.4).

Table 1: Survey of the forces on dust particles. Z **denotes the dimensionless charge,** q **the elementary charge,** R **the particle radius,** ρ **a mass density,** v **a speed,** $\vec{u}$ **a velocity,** σ **a collision cross section,** λ_{DL} **the linearized Debye length (eq. 22),** ℓ **a mean free path,** R_C **the Coulomb radius (eq. 23),** σ_{OML} **the collection cross section from eq. 24, and** m_i **the ion mass in** *amu*.

Force	Formula	Approximations	
Electrostatic	$\vec{F}_e = qZ_D\vec{E}$	$R \ll \lambda_D$	27
Neutral drag	$\vec{F}_n = -\dfrac{4}{3}\pi R^2 \rho_n v_{th,n}(\vec{u}_D - \vec{u}_N) = -K_{D-n}\Delta\vec{u}$	$R \ll \ell_n$ $\lvert\Delta\vec{u}\rvert \ll v_{th,n}$	28
Ion drag	$\vec{F}_i = (\sigma_{OML} + \sigma_{scat})\rho_i\vec{u}_i v_i$	$R \ll \lambda_D$	29
	$\sigma_{scat} = 2\pi R_C{}^2 \ln\dfrac{R_C{}^2 + \lambda_{DL}{}^2}{R_C{}^2 + \sigma_{OML}/\pi^2}$	$R \ll \ell_i$	30
	$v_i{}^2 = v_{th,i}{}^2 + \lvert\vec{u}_i\rvert^2\left[1 + \left(\dfrac{\lvert\vec{u}_I\rvert/v_{Bohm}}{0.5 + 0.05\ln\dfrac{m_i}{Z_i} + \sqrt{\dfrac{T_i}{T_e}}}\right)\right]$		31
Thermophoresis	$\vec{F}_{th} = -\dfrac{4\sqrt{2\pi}}{15}\dfrac{R^2}{v_{th,n}}\kappa_T\vec{\nabla}T_n$	$300K < T < 500K$	32
Gravitational	$\vec{F}_g = \dfrac{4}{3}\pi R^3 \rho_D\vec{g}$		33

In order to compare these forces, the order of magnitudes can be calculated. For 10 nm charged particles in a typical PECVD plasma before agglomeration (p = 1 mbar, T_i = 500 K (0.04 eV), T_e = 3 eV, $n_e = n_i = 10^{15}$ m^{-3}) the electrostatic force at the sheath boundary (E = 30 V/cm) is 6×10^{-13} N, the ion drag force in the bulk of the plasma 10^{-13} N, the neutral drag force for 100 sccm flow 10^{-17} N, the thermophoresis force (at a temperature gradient of 10 K cm^{-1}) 10^{-18} N, and the gravitational force 10^{-19} N. For neutral particles of 10 nm, the electrostatic force disappears and the ion drag becomes comparable to the neutral drag force.

1.2.5   Interacting dust particles

When the distance between dust particles is not anymore much larger than the Debye length, dust-dust interactions come into play. The most important consequence of a high dust concentration is the electron depletion, which is described by the Havnes parameter (section 1.2.2). At high dust concentration, dust particles cause a reduction of the electron concentration which in turn causes a reduction of the dust charge. This negative feedback limits the dust charge.

Dust particles at a very short distance (order λ_D) are not shielded completely and experience a strong repulsion. At medium distances another effect comes into play: the overlap of the two Debye spheres is energetically favourable, so that at $r > 2.73\ \lambda_D$ there exists an attractive force. These two effects sum up in a Lennard-Jones like potential. At long distances, the interaction asymptotically goes to a r^{-2} dependent repulsion. This interaction is lost at distances where ion collisions play a role ($r > \ell_i$).

Interaction potential

$$W_{int} = \frac{q^2 Z_D^2}{4\pi\varepsilon_0}\left(\frac{1}{r} - \frac{1}{2\lambda_D}\right) e^{-r/\lambda_D}$$

34

Interaction potential limit

$$W_{int} = \frac{q^2 Z_D^2 R}{8\pi\varepsilon_0 r^2}$$

35

The ion flux towards the dust particle can result in an extra drag force that acts as an attractive interparticle force. This called the ion shadowing force. The particles can spontaneously align themselves in linear chains, which is described by the wakefield attraction. In strongly interacting dust clouds, dust dipole-dipole interactions also become important. For a more thorough review of interparticle forces see [6,14,40].

These attractions can lead to crystal-like ordering of a dust cloud. The critical parameter here is the ratio between the dust interaction and kinetic energy. When the interaction energy takes over, interaction forces become important and the dust can arrange itself in an ordered structure.

Interaction parameter

$$\Gamma = \frac{q^2 Z_D^2}{4\pi\varepsilon_0 \langle r\rangle} e^{-\langle r\rangle/\lambda_D} \frac{1}{kT_D}$$

36

For the nanoparticles of interest, with a radius of 10 nm and a charge $Z = 1$, this interaction parameter can be estimated. For typical PECVD conditions (see section 1.2.4) and dust kinetic energy $kT_D \approx 0.03 eV$, the potential energy is already competing with the kinetic energy at a nanoparticle concentration of 10^{12} m^{-3}. A dust cloud in an ordered structure becomes less compressible, which can be described with an internal pressure [41]. Also the charging process of the nanoparticle is influenced by the dust interaction.

1.3 DYNAMICS OF DUSTY PLASMAS

1.3.1 Single dust particle dynamics

Isolated charged particles can only be levitated in regions where the electric field is sufficiently strong. This is the case in the pre-sheath and sheath regions of a PECVD plasma. The electric field in this region rapidly increases towards the electrode. This gives a large gradient of ion energy and ion/electron density ratio, reflecting in a range of dust charges.

Single particles can fluctuate around their equilibrium position. As the major contribution to the levitation force is the electrostatic force (section 1.2.4), the angular frequency ω of this fluctuation can be approximated linearly by $m_D \omega^2 = \mathrm{d}(QE)/\mathrm{d}x$, in which m_D, Q and E denote the dust mass, dust charge and the local electric field, respectively. This frequency can be measured and utilized to analyse the dust charge and electric field at several locations in the sheath [14]. For small oscillation amplitudes, the electric field can be approximated from Gauss' law (equation 38) and the natural frequency becomes [40]:

Single particle oscillation
$$\omega = \sqrt{\frac{Z_D}{m_D} \frac{n_i q}{\varepsilon_0}}$$
(37)

Observations have been done of spontaneous vertical oscillations of dust particles in low density plasmas (0.004 mbar). The theory behind this phenomenon is a fluctuation between position and charge: close to the electrode, ion concentration is lower so the particle gains a higher (negative) charge. Consequently, the particle moves away from the electrode and partially loses charge so that it again starts to move to the electrode. This mechanism is closely related to the charging process.

1.3.2 General PECVD plasma dynamics

The dynamics of a PECVD plasma can be modelled using computer simulation. Such a simulation is based on a set of equations, resembling the equations in hydrodynamics. These equations totally describe the behaviour of a *plasma fluid* as a whole using a certain model. The model that will be described in this section is a conventional model for PECVD [37,42–44].

The electric field is created by local charges and can be calculated using Gauss' law. In computer simulations, usually the potential is calculated instead of the electric field ($\vec{E} = -\vec{\nabla}V$) with the Poisson equation. In the following equation, the charge density is expressed in dust, electron and total ion densities.

Gauss' law
$$\varepsilon_0 \nabla \cdot \vec{E} = q(n_i - n_e - Z_D n_D)$$
(38)

For electrons and ions, there exists a *continuity equation*, which equates the change in concentration of a species to its flux, generation (sources), and destruction (sinks) of the particles. The particle flux is described by drift and diffusion terms. The diffusion is caused by a concentration gradient and includes the diffusion constant. The drift is described with a drift velocity. In this equation, n_j denotes the concentration, $\vec{u}_j$ the drift velocity, D_j the diffusion constant, and S_j the sum of all sources and sinks.

Continuity equation of species j
$$\frac{\mathrm{d}n_j}{\mathrm{d}t} + \nabla \cdot (n_j \vec{u}_j - D_j \vec{\nabla} n_j) = S_j$$
(39)

The ions are too heavy to react on the instantaneous radio-frequency field. To be able to describe the ion drift, an *effective electric field* can be defined [44]. This field directly gives the ion drift via $\vec{u}_j = \mu_j \vec{E}_{eff}$. In this equation, μ_i denotes the ion mobility and m_i the ion mass.

Effective ion E-field
$$\frac{\mathrm{d}E_{eff}}{\mathrm{d}t} = \frac{q}{\mu_i m_i}(E - E_{eff})$$
40

Next to the continuity equations, there exist energy conservation equations. Only two energy conservation equations are considered: one for the background gas and one for the electrons. Ions are assumed to dissipate all energy due to the high collisionality. The gas heat equation consists of the heat generated at the dust surfaces due to surface reactions (heat flux $\vec{J}_D$) and the heat generated by ion flux $\vec{\Gamma}_i$ in the direction of the electric field.

Gas heat equation
$$\nabla \cdot \left(-\kappa_T \vec{\nabla} T\right) = 4\pi R^2 n_D \vec{J}_D + \mathrm{e}\vec{\Gamma}_i \cdot \vec{E}$$
41

The equation of electron energy density ($w_e = \langle E_e \rangle n_e$), is much alike the continuity equation: the energy density change $\mathrm{d}w_e/\mathrm{d}t$ plus energy flux $\vec{J}_e$ is equal to sources and sinks (S_{we}). The extra term in equation 42 covers the energy gain by electron flux due to the electric field (also called *Ohmic heating*). The electron flux consists of a drift part that includes the electron mobility μ_e and a diffusion part with a diffusion constant D_e.

Electron energy density
$$\frac{\mathrm{d}w_e}{\mathrm{d}t} + \nabla \cdot \vec{J}_e = -\mathrm{e}\vec{J}_e \cdot \vec{E} + S_{we}$$
42

Electron energy flux
$$\vec{J}_e = \frac{5}{3}(\mu_e w_e \vec{E} - D_e \vec{\nabla} w_e)$$
43

Sources and sinks have to be identified before this model can be used. For the particle continuity equations (equation 39), these include gas in- and outflow, creation and destruction of particles by gas phase reactions, reactor surface reactions, and dust surface reactions. For the electron energy density equation (equation 42), these include the plasma power, electron impact reactions, and electron losses at the reactor and dust surfaces. The particle mobilities and diffusion coefficients are normally assumed to be constant.

To describe the dust particles, equations for charge and energy evolution are derived from particle and energy flux equations. The charge evolution is derived from OML theory (section 1.2.3); the temperature of the dust is calculated from three effects: heat resulting from electron-ion recombination, heat transfer to the background gas and radiative emission of heat [37]. The flux $\vec{\Gamma}_D$ of dust particles is the sum of drift and diffusion terms, in which the drift is divided by the damping constant K_{D-n} due to collisions with neutral gas particles.

Dust particle flux
$$\vec{\Gamma}_D = \frac{n_D}{K_{D-n}}(\vec{F}_e(\vec{E}_{eff}) + \vec{F}_i + \vec{F}_{th}) - D_D \vec{\nabla} n_D$$
44

All forces in this equation are further described in Table 1 on page 17.

1.3.3 Waves in dusty plasmas

In a PECVD plasma, an exchange can exist between the ion kinetic and electrostatic energy: the ion acoustic wave (IA). The restoring force is the electron pressure. When the dust concentration and charge influence the n_i/n_e ratio, the wave is called the dust-ion acoustic wave (DIA). The dispersion relation of this wave is given below, neglecting ion collisions and dust charge variations. For high wavelengths, $(\lambda_{IA} \gg \lambda_D)$ this wave can be approximated linearly with the dust ion-acoustic speed. Typical oscillation frequencies are 1-3 kHz.

Dust-ion acoustic wave
$$\omega_{DIA} = k \frac{\lambda_{D,e}\omega_{p,i}}{\sqrt{1 + k^2\lambda_{D,e}{}^2}} \simeq k \sqrt{\frac{T_e}{T_i}(P+1)}v_{th,i} \qquad\qquad 45$$

In this equation, ω_{DIA} and k denote the (angular) frequency and wavenumber, $\omega_{p,i}$ denotes the plasma frequency for ions (equation 2), $\lambda_{D,e}$ the Debye length for electrons, P denotes the Havnes parameter, and $v_{th,i}$ the ion thermal energy. The Havnes parameter describes the electron depletion with $P + 1 = n_i/n_e$. This dispersion relation reduces to the ion acoustic wave when $P = 0$.

A similar fluctuation can exist between dust kinetic and electrostatic energy: the dust acoustic wave (DAW). The restoring force here is the electron and ion pressures. Because of the much larger dust inertia, typical frequencies are in the 10-100 Hz range. In the approximation that these waves are much faster than the ions and much slower than the electrons, a dispersion relation applies that can be linearized for high wavelengths $(\lambda_{DAW} \gg \lambda_D)$:

Dust acoustic wave
$$\omega_{DAW} = k \frac{\lambda_D \omega_{p,d}}{\sqrt{1 + k^2\lambda_D{}^2}} \simeq k \sqrt{Z\frac{T_i}{T_D}}\sqrt{\frac{P}{P+1}}v_{th,d} \qquad\qquad 46$$

In this equation, $\omega_{p,D}$ and $v_{th,d}$ denote the plasma frequency and thermal velocity for dust particles.

In a collisional plasma, these waves are damped. Strong dust coupling and variation of dust charge impose extra complexities on these models: more information can be read in [6,14,40].

1.3.4 Void formation and instabilities

In strongly coupled dusty plasmas, many observations have been made on the formation of a central dust-free region in the plasma, called the *void*. This structure was particularly found in micro-gravity experiments on board the International Space Station, but also in ground based experiments. Especially when the gravitational force is balanced by a thermophoretic force, the dust cloud can exhibit three dimensional structures.

The void is created by ionization in the central region of the discharge. This results in a constant outward ion flow, which drags the dust particles outwards. This is balanced by the containing electrostatic force and can result in central dust-free region [6,37]. Dynamic phenomena of this void structure have been widely observed and are closely related to the dust growth mechanism.

Fluctuations in a strongly coupled dusty plasma have timescales ranging from minutes to milliseconds and can roughly be divided into three categories: the *generation instability* with frequencies in the order of 0.01 Hz, *void fluctuations* with frequencies of 10-100 Hz and a fast (kHz) fluctuation connected to dust ionization [45].

Generation instability

Slow fluctuations in dusty Ar:SiH$_4$ plasmas have been reported many times since the early 90s. Fluctuations in scattering signal and electron density were shown to go faster with gas flow rate and RF power [33,46]. This fluctuation was first explained as a competition between the dust-containing electrostatic force and the dust-expelling neutral drag force. As the first scales with R and the latter with R^2, the neutral drag force overcomes the electrostatic force after a certain particle growth time. The particles are then pushed away making space for a new nucleation of dust particles. Different size groups of particles were also observed in [47]; these groups were called *generations* of particles.

This effect was also studied in an Argon plasma with submersed carbon particles [48,49]. In these studies, it was possible to make spatial resolved pictures of the plasma, revealing the existence of a dust-free central void region in the plasma glow. A periodic fluctuation between a turbulence phase and a void phase was observed.

Recently, the generation instability in a silane plasma was addressed by observing the electrical parameters, scattering signal and light emission [50,51]. Both groups propose a mechanism in which particle nucleation is inhibited inside dusty regions because of very small precursor concentration: radicals are absorbed at the dust particles and the electron density is low so that only few negative ions are present. Only in the void there can be nucleation. When the dust particles grow inside the void, they push the previous generation outwards. Eventually a void appears in the new dust cloud and the process repeats itself. In this model, different generations of particles are spatially separated.

Void fluctuations

A void fluctuation is different from the generation instability, because it is not related to the subsequent generations of dust particles. In a void fluctuation the void exhibits a periodic movement. Recent developments in this area have been achieved in an Argon plasma with submersed sputtered polymer particles. A periodic fluctuation in current, emission, and scattering was found: a repeatedly contracting and expanding void was made visible with a high-speed camera and named the *heartbeat instability* [52]. This fluctuation of 10-40 Hz only occurred with a cloud of a "huge density of small dust particles". The characteristics of this instability were further elucidated with a high-speed camera in [53].

Also a fluctuation of 20-80 Hz has been observed in the third harmonic and in the plasma glow [54]. This fluctuation had a less ordered and a more ordered phase. The frequency of the fluctuation in the more ordered phase increased with increasing power and decreasing SiH$_4$ flow rate. The origin of the fluctuation was not elucidated, it was only stated that the more ordered phase was connected to the particle growth, the less ordered phase to expelled dust particles. An overview of these publications is given in [55].

1.4 PLASMA DIAGNOSTICS

1.4.1 Electrical diagnostics

External diagnostics (VI-probe)

It was noted in section 1.2.2 that a dusty plasma is more resistive due to more ion and electron collisions. Because of this, the dust aggregation can easily be detected by a non-intrusive electrical measurement. A conventional PECVD setup consists of an RF source, plasma chamber and a matchbox to match the impedances of both. The applied power is measured with an in-line power meter before the matchbox. In some setups, a special voltage and current probe is installed in between the matchbox and the powered electrode. In Figure 6, this setup is shown.
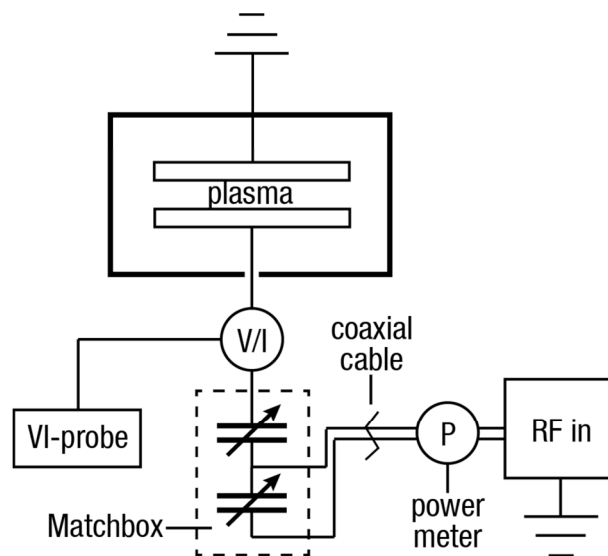
Figure 6: Electrical diagnostics on a PECVD discharge

The power meter cannot be used directly for plasma diagnostics, because of an unknown power dissipation inside the matching circuit. With a probe on the electrode side of the matchbox, this problem does not play a role so that the electrode potential, current and derived quantities can be directly measured [32]. Several diagnostics can be done with a VI-probe:

- The voltage-current phase shift is related to the concentration of dust particles [56]
- The constant (DC) voltage of the powered electrode, called the *bias voltage* or *self-bias* (see section 1.1.3) decreases when dust is formed. It has been reported that $\Delta V_{DC}/\Delta n_e$ and $\Delta n_e{}^2/\Delta V_{DC}$ scale linearly with dust radius and concentration, respectively [57].
- The third harmonic of the RF voltage was reported to increase in the same way as the *self-bias* decreases [45,56,58]. This quantity can also be used as a qualitative dust-monitoring observable.

Langmuir probe

Another electrical plasma diagnostic tool is the *Langmuir probe*: a thin ($\ll \lambda_D$) electrical probe submersed in the plasma. Although difficult to interpret, this is a popular technique because it is cheap and easy to operate. The difficulty of a probe in a dusty plasma is the fact that the probe disturbs the plasma potential, altering the dust and ion concentrations in its neighbourhood. Moreover, in a dusty plasma, the probe surface gets contaminated.

By biasing the probe to a negative potential, the probe can be cleaned during its 'off' time [12]. Several diagnostics with the Langmuir probe are described in literature:

- The ratio of saturation currents at positive and negative probe potentials is related to the electron-ion concentration ratio: $\frac{n_e}{n_i} = \frac{I_-}{I_+} \sqrt{\frac{m_e}{m_i}}$. When several ions are present, their relative densities have to be known for instance by mass spectrometry (section 1.4.3) [12,59]

- During the first phase of the plasma afterglow, the electrons cool down and the currents are only produced by the ions and negative clusters. Because quasi-neutrality still holds, the mass of singly charged small plasma clusters (up to 80 ion masses) can be measured: $\frac{m_D}{m_i} = \left(\frac{I_-}{I_+}\right)^2$ [12,60].

- From a full I-V characteristic of a Langmuir probe, plasma potential, electron temperature, electron density and ion density can be estimated [12,49].

- Electron photodetachment (see section 1.4.4) of clusters (< 2 nm) can be detected with a Langmuir probe, but this is more conveniently done with a microwave resonance technique [60]

- The plasma potential can be measured using an electron emitting probe. When the probe potential is below the plasma potential, electrons are emitted into the plasma, while when the probe potential is above the plasma potential, electrons are absorbed. At the potential that the probe current changes sign, the probe potential equals the plasma potential [12].

1.4.2 Light emission and absorption

Optical emission spectroscopy (OES)

Because of the large number of excited species inside a plasma, a significant amount of radiation is produced. With optical emission spectroscopy, the plasma emission spectrum is normally monitored in the near UV/visible range (200-800 nm).

Neglecting chemical reactions that produce emissive species, the number of emitted photons N_{ph} (in s^{-1} m^{-3}) by a certain transition can be related to the concentration of ground state species (n_g) and the concentration of electrons (n_e) [61]. The proportionality constant X_{eff} depends on the excitation cross-section and the branching ratio of an emissive de-excitation.

$$N_{ph} = n_g n_e X_{eff}(T_e) \qquad\qquad 47$$

The emission intensity gives information about concentrations of light emitting species, the electron density and the electron temperature. In a silane plasma however, there are many complicating factors: emission rate coefficients can be greatly influenced by chemical reactions that use or produce excited species, giving population or depopulation of certain excited states. Other complicating factors are extra collisions at higher pressure giving extra non-radiative decay, reabsorption and -emission of light, and transfer between energy levels in collisions of different gases. Also a direct intensity measurement always needs a calibration of the setup to a known intensity, which is difficult to achieve in a plasma chamber setup.

Therefore, only the most distinct emission energies can be used to extract information from the plasma and intensity *ratios* are most often used in combination with empirical relations. Common diagnostics with OES are listed below. A typical SiH$_4$:H$_2$ emission spectrum is shown in Figure 7 and the most important emissive

transitions are listed in Table 2, together with their wavelengths. The transitions are described in standard spectroscopic notation. The SiH transition is a transition between a molecular orbital close to Si (denoted with A) and an orbital close to H (denoted with X).

- The electron temperature can be determined by measuring Argon emission intensity [61] or by measuring the H_α / H_β ratio [62]. For silane plasmas, also the Si· / SiH· ratio can be used [63].
- The Si· emission intensity can be correlated to the deposition rate [64]
- The H_2 (Fulcher) lines can be used to measure the hydrogen concentration. The ratio between the Fulcher lines and the G_0B_0 hydrogen peak can be related to the electron temperature [25,65].
- The transition between nc-Si:H and a-Si:H growth can be related to the flux ratio atomic hydrogen/silicon species. This flux ratio can be determined by measuring the H_α / Si· ratio [64,66] combined with a correction factor [21,67].
- The emission profile of the plasma marks the α-γ' transition. By recording the emission profile, this transition can easily be detected, even with the naked eye [35]
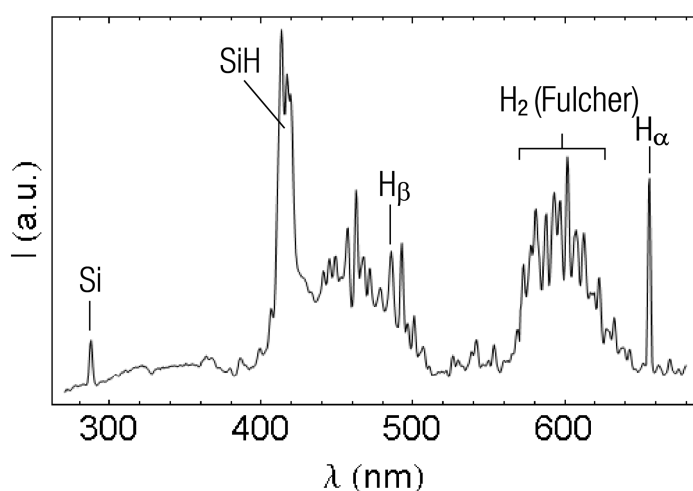

Figure 7: A typical silane-hydrogen plasma emission spectrum

Table 2: Transitions of silicon, hydrogen, and argon species [61]

Line	Transition	λ (nm)
Si	$4s\ ^3P_{0\text{-}2}$-$3p\ ^3P_{0\text{-}2}$	251-253
	$4s\ ^1P$-$3p\ ^1D$	288.2
	$4s\ ^1P$-$3p\ ^1S$	390.6
SiH	$A\ ^2\Delta$-$X\ ^2\Pi$	410-425
H_α	$3d\ ^2D$-$2p\ ^2P$	656.2
H_β	$4d\ ^2D$-$2p\ ^2P$	486.1
$H_{2,\ Fulcher}$	$3p\ ^3\Pi_u$-$2s\ ^3\Sigma_g$	595-630
$H_{2,}\ G_0B_0$	$3d\ ^1\Sigma_g$-$2p\ ^1\Sigma_u$	461-464
Ar	$4p_2\ [^1/_2]_1$-$4s\ [^3/_2]_2$	696.5

Laser induced fluorescence (LIF and TALIF)

Laser induced fluorescence (LIF) is technique that was especially used in the 90s. The experimental setup is a typical fluorescence setup with a light source (laser) parallel to the electrodes and a detector at 90° angle with the light source to detect fluorescence. Fluorescence in plasmas is often difficult to detect, as the plasma emission tends to dominate over the fluorescence signal. In dusty plasmas, the fluorescence technique is impossible to apply, as scattering at the dust particles increases strongly with increasing dust sizes. However, when a two-photon fluorescence technique is used (TALIF) the fluorescence signal is at a different wavelength and can be separated from the scattered signal [68].

The LIF technique is used mainly to directly detect the SiH· concentration [22,69]. It has also been used for the determination of the SiH_2· concentration [70], but due to interference of the plasma glow, the plasma had to be turned off shortly (several μs) during the measurement of several. Two photon absorption is used to detect atomic hydrogen: excitation at 205 nm followed by fluorescence at H_α. The wavelength of 205 nm (6 eV) can however also dissociate the silane molecule: predominantly Si_2H_6 dissociates giving extra energetic H species.

With a fitting technique on the Doppler width of the emission peak, the thermal and energetic H emissions can be separated giving information about concentrations of atomic hydrogen and disilane simultaneously [71].

Infrared spectroscopy (FTIR or ILSS)
Infrared spectroscopy technique in silane plasmas is mainly used to determine the SiH_4 density: hence the name Infrared Laser-based Silane Spectroscopy. An infrared beam crosses the plasma (or exhaust pipe) and the absorption is detected by a Fourier-Transform Infrared (FTIR) detector. The peak at 2189 cm^{-1} is used to determine the silane concentration. Because of an overlapping of different absorption peaks, the Lambert-Beer law cannot be used directly and a calibration on known silane concentrations is necessary [20,72,73]. From the silane concentration and silane inflow, the silane depletion can be calculated. Also the deposition rate can be estimated, assuming that all consumed silane ends at the substrate [74].

An extension of this technique adds a set of mirrors to increase the path length and so the detection limit. With this technique, all SiH_x radical concentrations can be detected simultaneously [17,75].

Laser-induced heating and evaporation (LIPEE)
When a laser beam of high power encounters a solid particle, it causes rapid heating, black-body radiation and eventually vaporization. The produced radiation can be used as a particle sizing technique. This technique was important in the development in the silicon particle growth mechanism [76]. Using an assumption on the decay rate of the radiation, particle size and concentration can be deduced.

A more elaborate overview of current optical techniques of nanoparticle detection can be found in [77].

1.4.3   Mass and energy spectroscopy
Mass spectroscopy is a sophisticated technique to detect ions and neutral species. Particles are extracted from the plasma or plasma afterglow and separated on molecular mass. Also particles can be separated on velocity: in this way ion energy distribution functions (IEDFs) of separate ion species can be obtained.

An experimental setup conventionally consists of an ionization chamber, ion extraction optics, an electrostatic analyser and a quadrupole mass spectrometer. Neutral species are ionized with high energy electrons in the ionization chamber; for ion analyses, there is no extra ionization process. The extraction optics focuses the ions in a single beam. In the electrostatic analyser, a certain ion energy is selected and in the mass spectrometer, the particles are separated on their m/Z (mass to charge) ratio.

A crucial part of the setup is the particle extraction. The conventional extraction method is from the side of the plasma, a few cm away from the electrodes. An aperture (100-300 μm) admits incoming particles into the ionization chamber, after which they are collected by the ion extraction optics [59]. Negative species can only be collected in this way during the plasma afterglow or during the off-time of a pulsed plasma, because they are normally contained within the plasma [26].

Particles can also be collected via a small orifice (10-30 μm) in the grounded electrode. In this way the composition of depositing particles can be detected directly. Using a positive potential, negative particles are extracted during the discharge, however the potential influences the local plasma properties. Concentrations and energy distributions of positive and neutral species in the plasma sheath can be determined directly [78].

The mass detection range is determined by the quadrupole filter and normally ranges from 1 to 40 silicon atoms. However, with an sophisticated detectors, particles with sizes up to 100 nm can be detected [12].

1.4.4 Microwave diagnostics

Microwave techniques are all based on the interaction of microwaves with the electron gas inside the plasma. The frequency of microwaves is in the order of the electron plasma frequency (section 1.1.1) and therefore the electron density influences the microwave. Dust is not influenced by the microwaves: their movement is too slow compared to the microwave frequency (GHz) and too small compared to the microwave wavelength (cm).

In PECVD, two types of microwave measurements exist: interferometry and cavity resonance/ringdown. Interferometry is based on the phase shift of the wave passing through the plasma, which is influenced by the electron density. This technique is sensitive down to an electron concentration of 10^{16} m^{-3}. For lower concentrations (10^{12}-10^{16} m^{-3}), a standing wave can be generated inside the plasma chamber. The chamber acts as a microwave cavity and from the resonance frequency shift, the electron density can be derived [12].

<u>Photodetachment/ionization</u>

A powerful analysis method that combines light spectroscopy with cavity resonance has been developed. This technique is based on light induced detachment of electrons and is called *photodetachment* (for negative ions) or *photoionization* (for neutrals). Light with specific detachment or ionization energy is used to irradiate the plasma so that electrons, which are relatively easy to detect, are released. An increase of electron density is detected with a microwave cavity. The increase directly gives the concentration of the irradiated species. Electron detection can also be done with an electric probe (section 1.4.1).

With this technique a selective detection is possible, due to different detachment energies of different ions. Moreover, the electron affinity of a nanoparticle changes with its size, so that information about the size and charge distribution of the nanoparticles could be obtained. There were no reports of this technique found in the last decade, although the technique was found to be promising especially for nanometre sized particles [12].

1.4.5 Light scattering

When a dust particle interacts with radiation, it can absorb and re-emit the light: an incoming wave sets the dielectric particle in oscillation, which in turn sends out the radiation with (on average) no preferred direction. This scattering process diffuses the light. As this effect is proportional to the radius of the particle to the sixth power, this effect can only be implemented to detect the largest dust particles in the plasma. When this technique is used as a plasma diagnostic, it is called *laser light scattering* (LLS).

When the radius of particles is much smaller than the wavelength of the incident light, which is the case for nanoparticles, the scattering phenomenon is called *Rayleigh scattering*. The scattering intensity of a single Rayleigh scattering particle is as follows [12,79]:

$$I_{scat}(\theta) = I_0 \frac{8R^6}{\lambda^4 r^2} \left| \frac{m^2 - 1}{m^2 + 1} \right|^2 (1 + \cos^2 \theta) \qquad 48$$

With I_0 the intensity of the incoming beam, R the radius of the particle, λ the wavelength, r the detector distance from the plasma and m the ratio of indices of refraction n_{dust}/n_{medium}. The scattering is optimal in

the forward direction (0° angle with the incident beam). At 90°, the scattering is a factor 2 lower. However, because it is experimentally difficult to subtract the stray light from reflections of the incident beam on the plasma chamber, experiments are often done at 90°. As is visible in Figure 8, the scattering intensity is extremely low for few nm sized Si nanoparticles. Therefore, the number of scattering particles has to be very high (> 10^{15}-10^{16} m^{-3} [17,80]) in order to obtain a detectable scattering signal.

To determine size and concentration of nanoparticles from a scattering experiment, the scattering signal during the plasma afterglow can be monitored. Using an assumption on the thermal aggregation process (section 1.2.1), both concentration an size can be deduced [80].

For larger particles, the more complicated Mie scattering theory is applicable. From the angle-dependent Mie scattering signal, particle densities and sizes can be determined. Also a technique with simultaneous scattering of 2 wavelengths is developed, with which spatial dust profiles can be deduced [60].
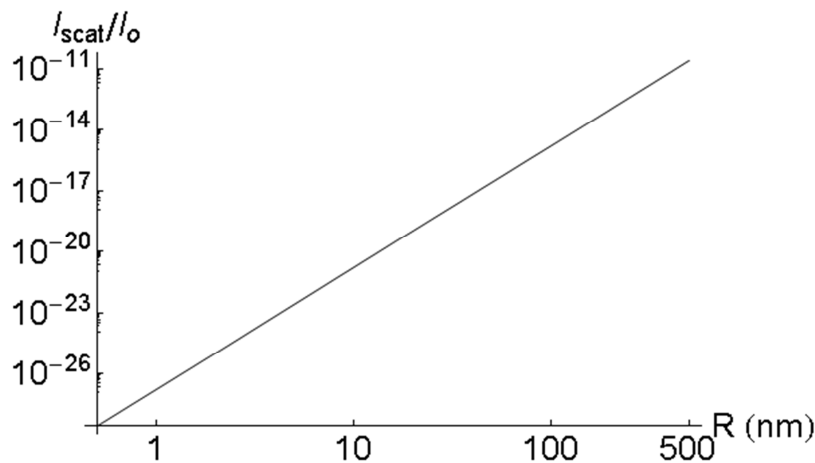
Figure 8: Theoretical Rayleigh scattering for silicon nanoparticles ($m = 4.5$) at 90° and 15 cm distance at He-Ne laser wavelength

1.4.6   Ellipsometry

Ellipsometry is a technique that uses polarized light to model the dielectric function of a deposited thin film. As it is an optical technique, it does not perturb the deposition and can be used *in situ* to follow the growth process. In general, when a linear polarized wave reflects on a certain angle, the polarization is changed to an elliptical polarization (hence the name *ellipsometry*). By examining the incident and reflected wave, two reflection coefficients can be calculated: for polarizations parallel (r_p) and perpendicular (r_s) to the light plane. The ratio between these quantities is called the *complex reflectance ratio ρ*, which can be expressed in the phase shift Δ and amplitude ratio upon reflection $\tan \Phi$.

Complex reflectance ratio
$$\rho = \frac{r_p}{r_s} = \tan \Phi \, e^{i\Delta}$$
49

In order to convert the complex reflectance ratio into material properties, a certain model is used which is fitted to the wavelength-dependent complex reflectance ratio using a minimization algorithm. From the fitting parameters, information like the band gap energy and layer thickness can be derived.

A model often used for amorphous semiconductors is the model by Forouhi and Bloomer [81]. For mixtures of crystalline/amorphous phases a more complicated model is used: the Bruggeman effective medium approximation (BEMA) combines the two dielectric functions of both materials [82].

1.4.7 Imaging techniques

Imaging techniques have been widely used to study the dynamics of dusty deposition plasmas. These techniques make 2D images of the plasma and thus provide a convenient method to study the plasma dynamics. Optical emission and scattering are the two phenomena that are mostly combined with imaging. It is also possible to make 2D pictures of black-body radiation by laser induced heating [77].

In the simplest setup, a camera is used to monitor a wavelength band of the plasma emission. This technique is sometimes called *spatiotemporal optical emission spectroscopy*. Using a mathematical technique (Abel inversion), a 2D picture can be converted to a radial image of the plasma emission [83].

A scattering imaging setup for the detection of small nanoparticles (1-10 nm) requires a laser beam of high intensity and good scattering properties: typically a >1 W Argon ion laser (488 nm) is used. The laser beam is expanded in one direction and polarized. The resulting polarized laser 'sheet' is aligned between the electrodes and a (high speed) CCD camera is mounted at an optimum angle for the detection of particles [84,85]. Because of large plasma emission, the scattered signal can be difficult to separate, even with a small band-pass filter at the laser wavelength. To overcome this problem, the plasma can be pulsed and the scattered signal is recorded during the afterglow [86].

Chapter 2   Experimental

2.1   PLASMA CHAMBERS

Two PECVD setups available in the Utrecht Solar Energy Laboratory were used in this thesis. These two setups are described in this section.

2.1.1   IRIS

The PECVD system IRIS (Ions and Radicals in Silane plasmas) is a deposition system consisting of one reactor, similar to the reactors in ASTER that are described below. The IRIS system is used purely for plasma diagnostics: with one large viewport in front and two smaller on the sides, there are many possibilities for optical experiments. On the grounded electrode, where normally substrates are mounted, there is a 10-30 μm orifice giving entrance to an energy resolved mass spectrometer. Figure 9 is a technical drawing of the IRIS reactor. The IRIS system is described in more detail in [87]. The reactor volume of IRIS is 9.30 L.

The electrical system consists of a 50 MHz power supply and an L-type matching network (Figure 10). A plasma is obtained in several steps. First a constant gas flow is established using a set of mass flow controllers and the reactor pressure is stabilized with a valve in the gas outlet. Then RF power is switched on and the plasma is ignited with an electrical sparker. Finally the reflected power, which is measured with an in-line power meter, is minimized to obtain the best applied power. This is done by changing the capacitance of the two variable capacitors in the matchbox.
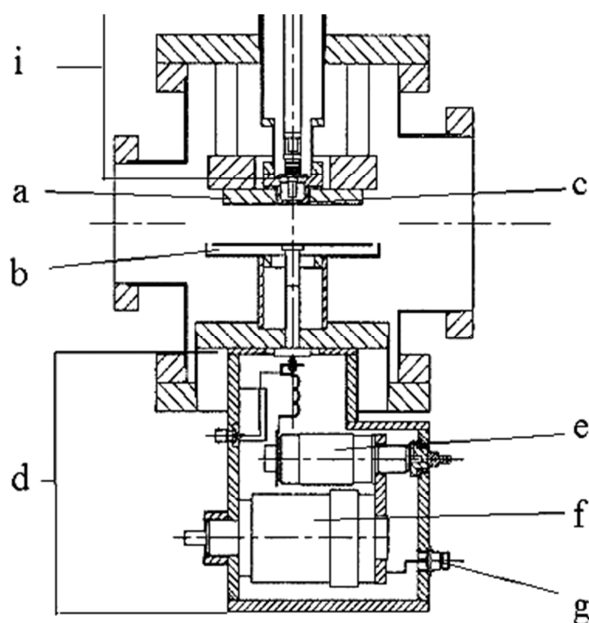
Figure 9: Technical drawing of the IRIS deposition chamber. The grounded electrode (a), powered electrode (b), orifice (c), matching network (d) with variable capacitors (e, f), power input (g) and mass spectrometer inlet (i) are depicted.
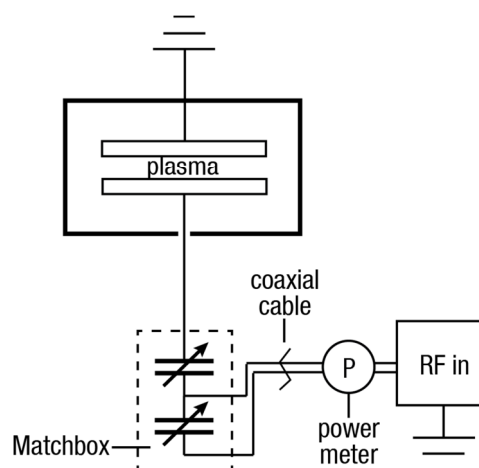
**Figure 10: RF power source and matchbox of IRIS**

2.1.2 ASTER

The ASTER (Amorphous Semiconductor Thin film Experimental Reactor) is a multi-chamber PECVD deposition system. The layout of the ASTER is depicted schematically in Figure 11. The system consists of five deposition chambers, a parking chamber, a load lock chamber, and a central chamber with a robot arm to load and unload the samples while they stay in the vacuum.

Only chamber 1 (and sporadically 4, which is identical) was used in this thesis, as it is equipped with a viewport for optical diagnostics and a MKS VI-probe for electrical diagnostics (see Figure 6 on page 23). Chambers 1 and 4 have special 'showerhead' electrodes, through which the gas is supplied into the chamber in a homogeneous way. The inter-electrode distance is adjustable between 5 and 27 mm. See Figure 12 for a schematic drawing. More technical information about the ASTER can be found in [21].
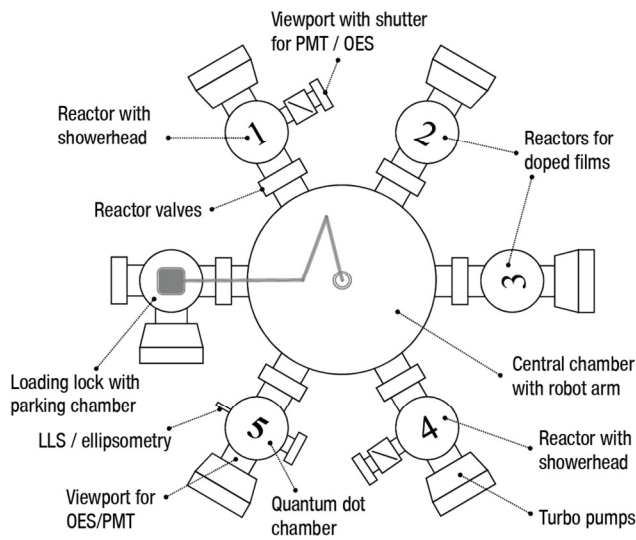
Figure 11: Schematic top-view of the ASTER multichamber PECVD system.
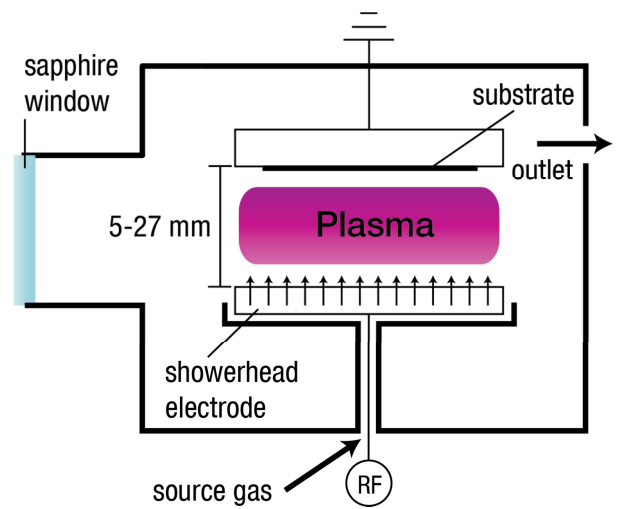
Figure 12: Schematic drawing of chamber 1

2.1.3 Standard deposition regimes

Experiments were done in deposition regimes commonly used in the USEL. The parameters will be referred to using the name in the first column, in the result section given in parentheses. The flow rates are given in cubic centimetre per minute at standard atmospheric temperature and pressure (sccm).

Table 3: Standard deposition regimes

| Name	Chamber	f (MHz)	T (°C)	p (mbar)	P (W)	SiH_4:H_2 (sccm)	d (mm)
a-Si (temperature)	IRIS	50	180	0.16	5	25:125	27
μc-Si (temperature)	IRIS	50	170	3-0.6	17.5	5:100	27
γ'-regime (emission)	ASTER 1	60	180	3	17.5	5:100	10
α-regime (emission)	ASTER 1	60	180	0.16	5	35:175	27
dusty (scattering)	IRIS	50	100	0.16	17.5	30:30	27
dust-free (scattering)	IRIS	50	180	0.16	5	5:125/25:125/30:175	27

2.2 OPTICAL EXPERIMENTS

The light emission and scattering experiments were done with a Hamamatsu *H5783-04* photomultiplier tube (PMT) as detector. The PMT was fastened inside a casing with an interference filter attached to the optical opening. The current output signal was converted to a voltage output signal with a parallel resistor of 100 kΩ. The gain of the PMT was adjustable using a variable resistor and was monitored with a multimeter. The signal was recorded using a National Instruments BNC-2110 interface connected to a NI DAQ 6013 data acquisition computer card. The maximum data acquisition speed with this setup was 20 kHz.

By choosing an appropriate filter, emissive transitions from certain species could be detected specifically. The applied filters for specific lines are given in Figure 13.


Filter type	λ (nm)
SiH*	413.8
H$_\alpha$	656
H$_\beta$	487
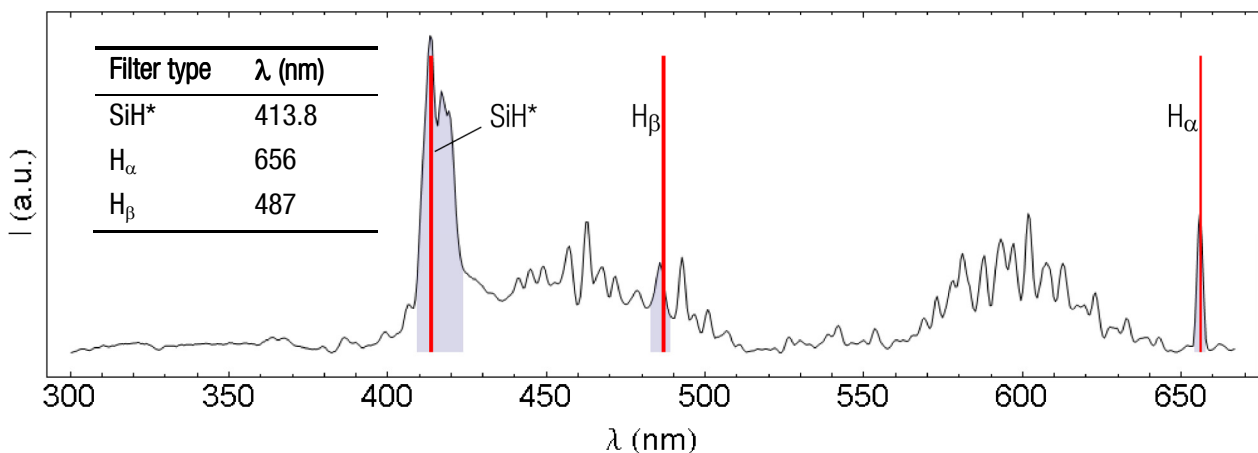
Figure 13: Bandwidths of the interference filters in an OES spectrum of a SiH$_4$:H$_2$ plasma in the γ'-regime. In the inset, the wavelengths of the filters are listed. The emission peak wavelengths can be found in Table 2 (p. 25).

The optical emission was detected using two setups. In setup A (Figure 14), two slits were used to be able to distinguish radiation originating from the plasma bulk and radiation from the sheaths. In setup B (Figure 15), a focusing lens was used so that the maximum intensity could be reached, increasing the signal to noise ratio of the PMT. In both setups, the optical part was shielded with a casing of black velvet on cardboard and wrapped by an extra black cloth.
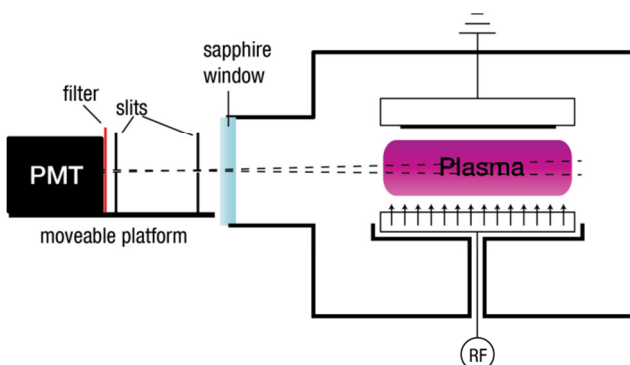
**Figure 14: Optical emission setup A with two slits selecting a specific height**
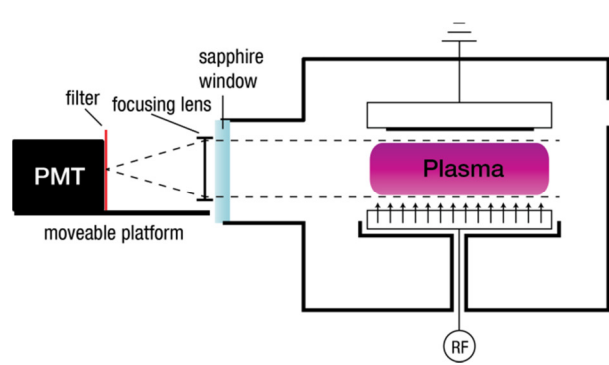
Figure 15: Optical emission setup B with a focusing lens

2.2.1 Detector height

The height profile of the optical emission in setup A was measured with a plasma in the γ'-regime. The results are depicted in Figure 16. As the electrode distance was 10 mm, the electrodes were estimated to be on heights 5 and 15 mm. All measurements with setup A were taken at 10 mm (plasma bulk) or 6 mm (plasma sheath).
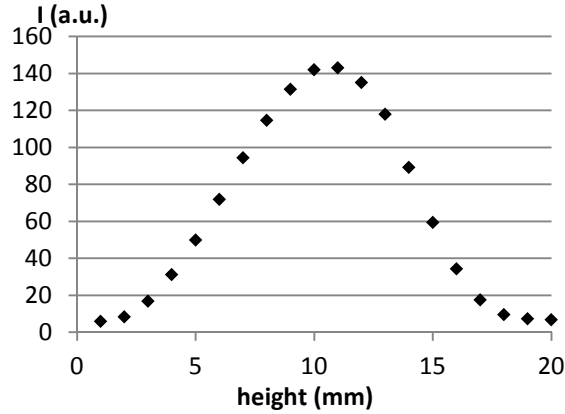
Figure 16: Emission intensity (H$_\alpha$) versus detector height in setup A

2.2.2 Spectrometer

The spectrometer *Avantes Avaspec-2048-USB2* equipped with a grating of large spectral width (200-1200 nm) was used or full spectrum measurements. The light from the plasma chamber was focused on an optical fibre placed at the position of the PMT in Figure 15, which subsequently led the light into the spectrometer. The minimum integration time of this spectrometer was 1.1 ms.

The spectrometer was connected to a PC with a USB cable. The standard *National Instruments* Labview program delivered by Avantes was optimized to be able to use data acquisition times of 5, 3 and 1.1 ms. Because of computer memory limitations, the maximum measuring time at 1.1 ms acquisition was 10 seconds (approx. 10000 spectra).

2.3 ELECTRICAL MEASUREMENTS

The electrode potential V, plasma current I and relative phase φ could be measured directly using an *MKS VI-probe* built between the matchbox and the powered electrode of ASTER chamber 1 (see Figure 6 on page 23). The plasma impedance ($Z = V/I$) and delivered power ($P = VI\cos\varphi$) were also calculated by the VI-probe. The probe was connected with a serial cable to the computer and the data acquisition was done with computer software by *MKS* at a maximum rate of 7.5 ms. Some data points were omitted by the program. In order to be able to take a Fourier transform, missing data points were inserted afterwards by duplicating adjacent points.

2.4 TEMPERATURE CALIBRATION

2.4.1 Preparation of thermocouples

Thermocouples were made from standard chromel/alumel wires (type K) [88]. Pairs of wires were knotted together and each wire was put through a glass fibre protecting mantle. Two thermocouples per substrate were attached: one in the middle and one 5 mm from the side. The used glue (*Vishay M-Bond 610*) was annealed under constant nitrogen flow at 135 °C for 3 hours (polycarbonate substrates: 115 °C for 6 hours).

2.4.2 Temperature interface

After mounting the substrates on a sample holder, the thermocouple wires were led outside the plasma environment to a special thermocouple throughput, which was mounted inside a CF25 access port. Outside the vacuum, the wires were connected to standard copper wires, so that the cold junction occurred at the room-temperature side of the throughput. The potential generated by the temperature difference was measured with a *National Instruments BNC-2110* interface connected to a *NI DAQ 6013* data acquisition PCI card. The software *Labview Signalexpress* had an acquisition speed of 1 kHz and took block averages of 1000 samples, effectively giving 1 point per second. The software converted the potential directly to a temperature using a cold junction temperature of 19.6 °C (room temperature measured with a thermometer).

2.5 SCATTERING EXPERIMENTS (LLS)

The scattering setup was tested in the IRIS, to be eventually implemented in the fifth chamber of ASTER.

A 15 mW He-Ne laser (632.8 nm) of type *05-LHP-151* was mounted on a height adjustable plate, which was attached to a viewport of IRIS. Behind the viewport, a collimator was inserted: a CF16 tube with a series of three blackened copper discs. The discs were aligned on their central opening (diameter: 1 mm). At the opposite side, a beam stop was glued onto a viewport. This beam stopper was made from graphite plates of 1 cm^2 (thickness: 1 mm). One plate acted as beam stopper, two plates with a central hole (diameter: 3 mm) were stacked onto this plate to reduce stray light and 4 were attached to the sides of this stack. See Figure 17 for a schematic.

The detection of scattered light was done both at short angle and at a 90° angle with the Hamamatsu *H5783-04* photomultiplier tube attached to the acquisition system described in section 2.2. The plasma glow was filtered with a small band pass 632.8 nm interference filter and the intensity was increased with a focusing lens. The setup is depicted schematically in Figure 18. All optical elements were shielded from ambient light by cardboard coated with black velvet.

The scattering setup test measurements were carried out as follows: 1) laser on 2) plasma on; wait 30 s to reach a steady state 3) 20 s acquisition time 4) plasma off 5) acquisition of after another 20 s. The scattering signal was obtained by subtracting the signal without laser illumination (average of last 20 seconds) from the signal with illumination (average of first 20 seconds).
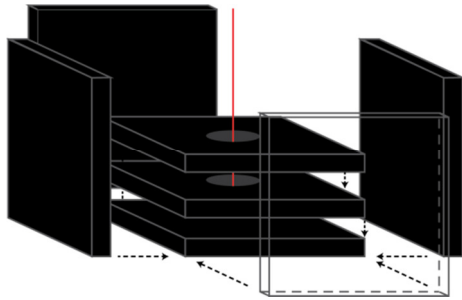
Figure 17: Schematic of the beam stop. All plates have dimensions 10x10x1 mm.
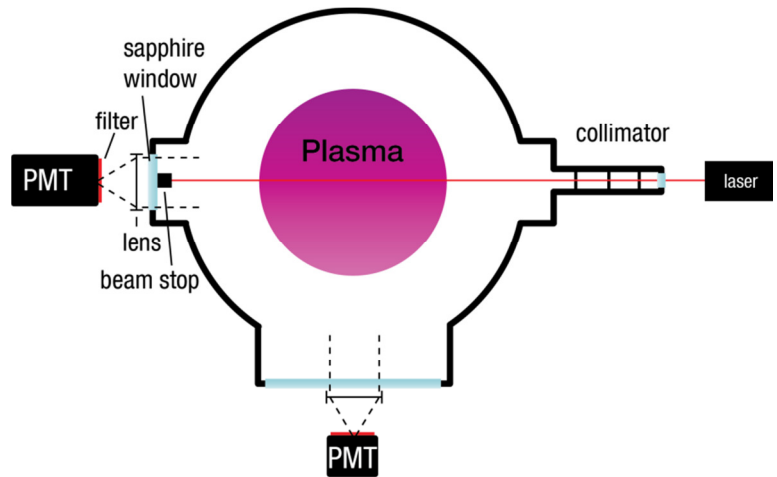
Figure 18: Top view of scattering setup. Both the short angle detection (left) and the 90° detection (bottom) are shown.

Chapter 3   Results

3.1   DUSTY PLASMA FLUCTUATION

In all optical emission experiments on a silane/hydrogen plasma in the γ'-regime, a stable oscillation in the emission intensity was observed. An example of such an oscillation in the SiH emission is shown in Figure 19. In order to quantify this oscillation, a discrete Fourier transform was done (Figure 20). The same fluctuation frequency was found in emission measurements of the H_α and H_β peaks and also in full spectrum measurements (see section 3.1.4). For comparison, the same measurement was done in the α-regime (Figure 21). The α-regime was found by visual inspection of the plasma emission profile. In this emission measurement no fluctuation was detected except for a weak signal at 50 Hz, which is the line frequency that is identifiable in all measurements. The complete parameters of the used plasma regimes are summarized in Table 3 on page 31.

Also the VI-probe was used to measure the fluctuation in the potential, current and impedance of the plasma. In all these observables, the fluctuation was reproduced (see Figure 22). Compared to the fluctuation in the emission, the relative amplitude of the electrical fluctuations was one order of magnitude lower.
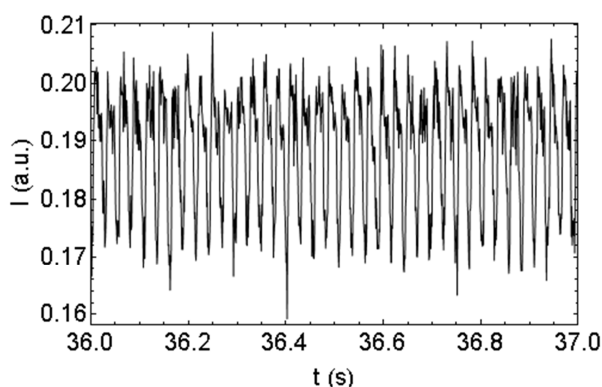

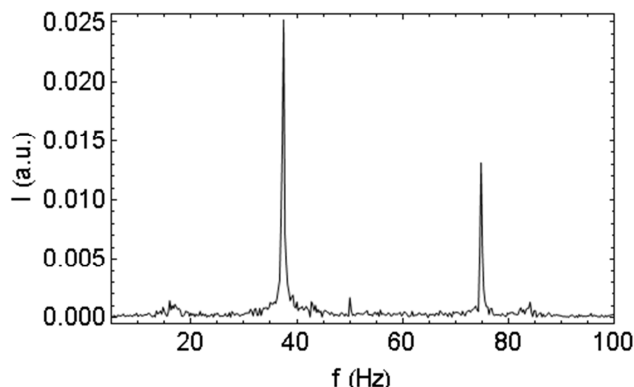Figure 19: Emission intensity of SiH in γ'-regime (#29)

Figure 20: DFT of SiH intensity in γ'-regime (#29)
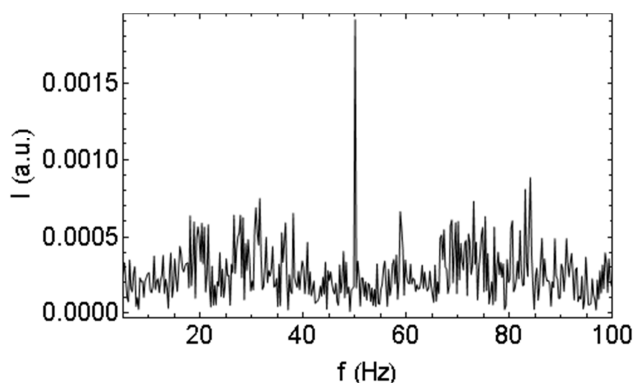

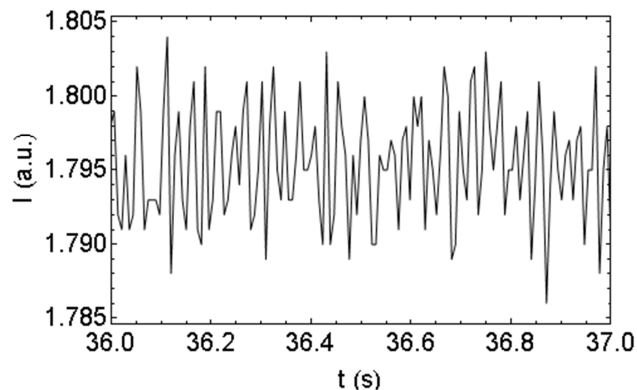Figure 21: DFT of emission intensity in α-regime (#26). Only the line frequency is visible.

Figure 22: Current through the plasma in γ'-regime (#29)

In order to examine the fluctuation in a consistent way, an analysis method was developed. Using this method, the fluctuation in optical emission and plasma current was measured in a heater temperature series and a gas flow series. Also an analysis of the full optical emission spectrum was done to measure all peaks simultaneously.

3.1.1 Discrete Fourier transform

A Fourier transform is a mathematical operation that can be used to transform a function on a time domain to the corresponding function on a frequency domain [89]. A discrete Fourier transform or DFT transforms a discrete function, for instance obtained by sampling a signal, to its corresponding frequency representation. The integrals in a Fourier transform change into sums and the discrete Fourier transform $\mathcal{F}(u)_s$ of dataset u_r can be calculated with the following formula. In this formula, datasets range from $r = 1$ to N and $s = 1$ to N.

$$\mathcal{F}(u)_s = \frac{1}{\sqrt{N}} \sum_{r=1}^{N} u_r e^{\frac{2\pi i (r-1)(s-1)}{N}} \qquad 1$$

This operation gives a series of complex values, which is the DFT. The frequency belonging to point with coordinate s is $(s-1)/N$ in units of the reciprocal sampling time. The intensity of the fluctuation can be found by taking the absolute value of the DFT. The angle of the complex number gives the phase of the fluctuation.

A non-sinusoidal fluctuation in the data results in a series of *harmonics* with frequencies that are an integer number times the ground frequency. The relative intensities of these harmonics determine the shape of the fluctuation.

When the time-resolution of the dataset is in the same range of the frequency of the fluctuation under investigation, an important DFT artefact called *aliasing* has to be considered: a set of data points on a sinusoid can always be fitted with sinusoids with a higher frequency (see Figure 23). To be specific: when a fluctuation of frequency f_{DFT} is found in a DFT of a data series with sampling frequency f_s, this fluctuation could indicate any $f_{\pm n} = nf_s \pm f_{DFT}$. Effectively, all fluctuations in the data with frequencies higher than half the sampling frequency (also named the *Nyquist frequency*) are folded back unto the spectrum. Also aliases of harmonics can be present. The graph in Figure 24 shows that a signal at 0.7 f_s has aliases at 0.3, 0.7, 1.3, 1.7, 2.3 and 2.7 f_s.
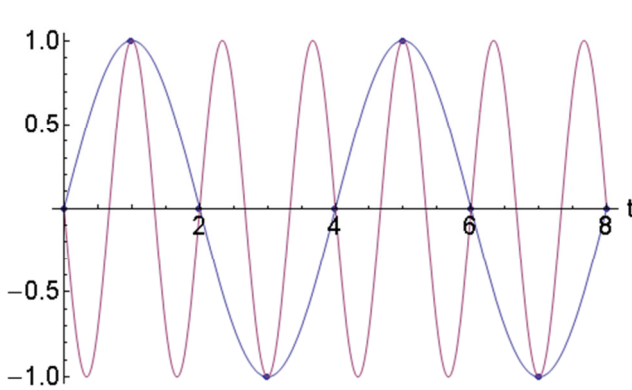
**Figure 23: Points on a sinusoid can be fitted by a different sinusoid.**
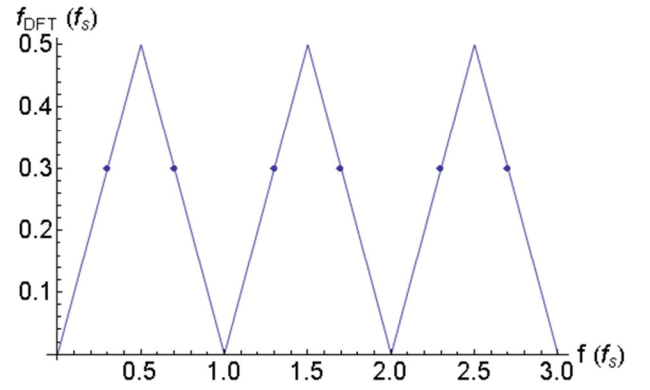
Figure 24: Aliases of a DFT signal with frequency 0.7 f_s.

3.1.2 Analysis method

Each measurement at certain plasma conditions and a certain emission wavelength consists of two data series: the emission series (Figure 19) and the current series (Figure 22). Of both series, the first 100 s after plasma ignition was divided into 25 blocks of 4 seconds. Each block was subjected to a discrete Fourier transform. The complete series of Fourier transforms is made visible as a density plot in Figure 25. As the VI-probe has a sampling frequency of ca. 133 Hz, the current DFT had a Nyquist frequency of 67 Hz. Frequencies above this

limit are displayed as a mirror image of those below, to be able to detect aliases. An example is the line in the VI-probe spectrum at 48 Hz. Because this line has a mirror image above the line at 85 Hz, it can be assigned to the 6th harmonic in the emission DFT. The same reasoning can be done for the line at 20 Hz (8th harmonic).
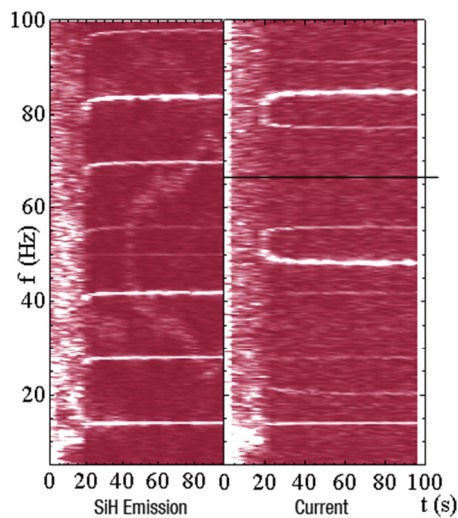

Figure 25: Series of DFT's. The data in the current DFT above the line are a mirror image of the data below the line to detect aliases (#27).
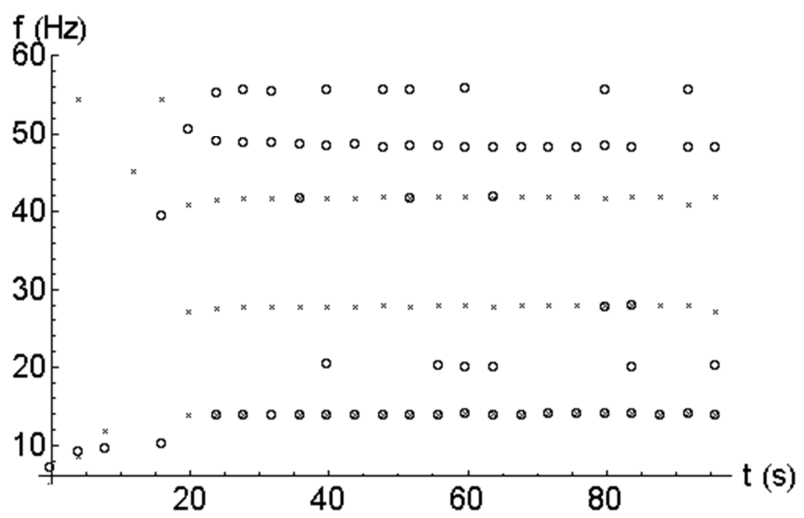
Figure 26: Detected peaks from the emission (crosses) and current (circles) frequencies in the range 5-60 Hz (#27)

The DFTs were analysed in a frequency range of 5-60 Hz. The peaks in each DFT were localized by looking for the 4 non-neighbouring maximum values inside each DFT. Starting from these maxima, Lorentz peaks were fitted locally using a least-squares algorithm. The resulting peak centres from both the emission and the current data were combined (Figure 26) and the lowest frequency occurring in both the DFT's was averaged resulting in a series of 25 frequencies in time intervals of 4 s. Finally, these frequencies were averaged over the stable plasma period, which started at 15-40 seconds, depending on the plasma parameters.
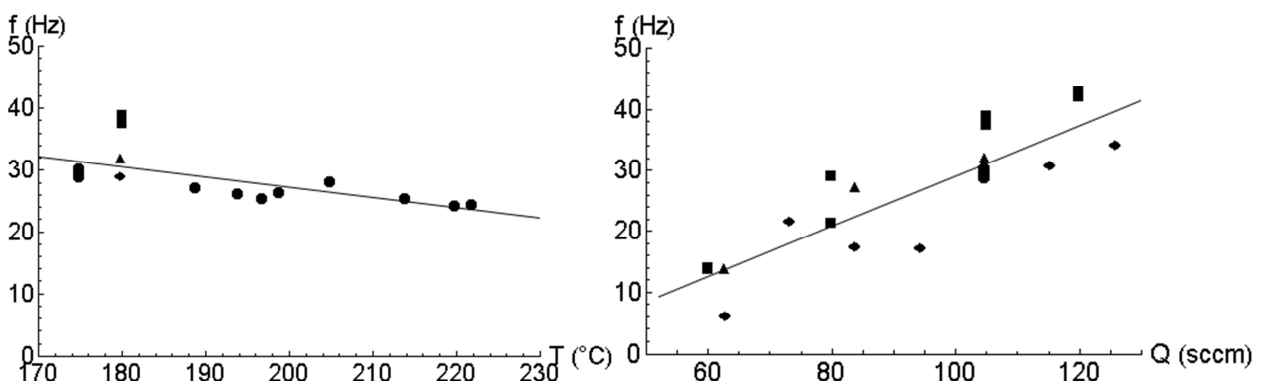
Figure 27: Plots of the fluctuation frequencies versus (left) heater temperature at Q = 105 sccm and (right) total flow rate at T = 175-180 °C. Displayed are a temperature series on H$_\alpha$ and SiH with optical emission setup A (discs), a flow rate series on H$_\alpha$ and SiH with optical emission setup A (squares), a flow rate series on H$_\alpha$ with optical emission setup B (diamonds), and data from the OES (triangles). The solid lines are linear regressions on all displayed data.

3.1.3 Results

The described procedure was done on measurements in a series of four different substrate temperatures and two series of different gas flow rates. The complete results can be found in Appendix A. Plots of frequency versus temperature and frequency versus total gas flow are shown in Figure 27. Different measurement sessions are displayed: temperature and flow rate series on H_α and SiH with optical emission setup A, flow rate series on H_α with optical emission setup B, and spectrometer measurements.

3.1.4 Optical emission spectrometer

In order to see the relative phases of the fluctuations of H_α and H_β and to observe the electron temperature, a fast series of spectra (1 to 5 ms per spectrum) was taken with the OES setup. These spectra were analysed in the following way.

First the baseline was subtracted from the spectra by a fitting procedure. As each measurement consisted of a series of spectra with the same baseline, the fitting was done on the average of all spectra in the same series. This baseline was then subtracted from every separate spectrum in this series. The fitting function had the form $f(\lambda) = a + b \log \lambda$, with λ the numerical value of the wavelength in nanometers. The parameters a and b were found using a least squares method with an adapted norm function. Whereas the standard least square algorithm minimizes the norm $(u_\lambda - f(\lambda, a, b))^2$, the adapted method replaces this norm function on one side by a linear function starting from a certain 'cut-off' value. The adapted norm function is displayed in the inset of Figure 28. The used values for the cut-off and line slope were 1 and 0.1, respectively. In this way, the points deviating above the baseline contribute far less to the error of the fit and the baseline is fitted almost through the lowest points.
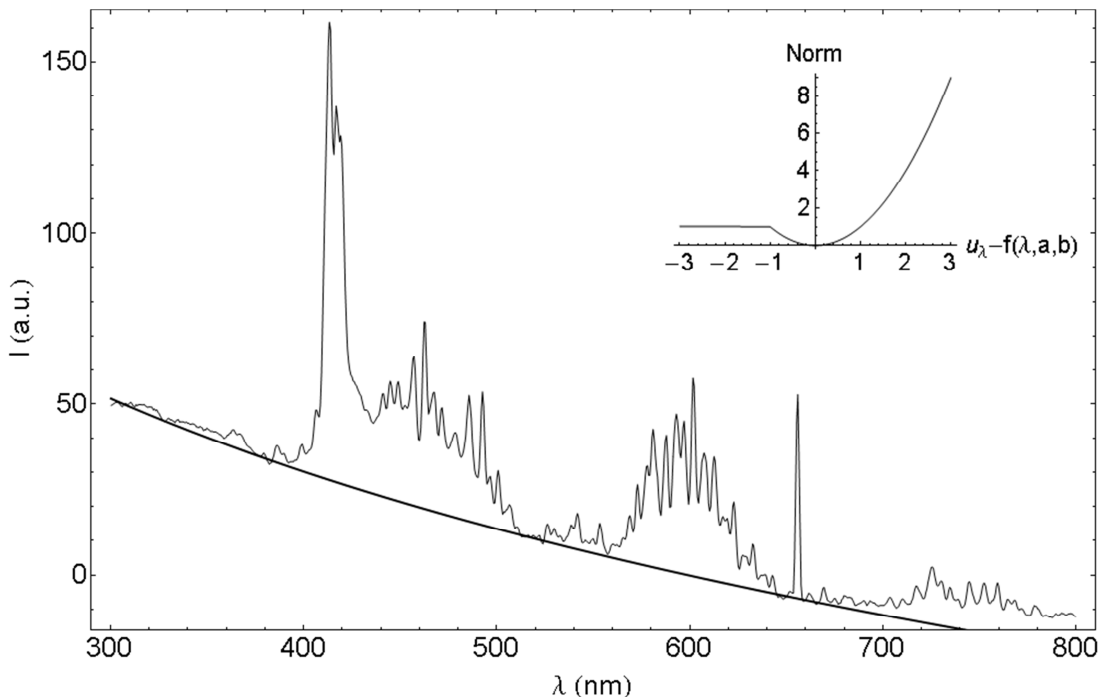

Figure 28: Averaged spectrum with fitted baseline. Inset: adapted norm function used in the baseline fitting procedure.

After subtracting the baseline, the H_α and H_β peaks in the average of the spectra in one series were fitted using a procedure based on the one used in [21]. The H_α peak could be fitted with a single Gaussian. However, the H_β

peak overlaps with neighbouring peaks. To obtain the H_β peak area, the sum of five Gaussians is fitted with a least squares method starting from initial λ values of 478, 486, 493, 497, and 501 nm (Figure 29). The surface of the peak at 486 nm is the H_β emission intensity.

The deviation from these peaks will result in the fluctuation. The deviation of each separate spectrum in one series was calculated by taking the integral between the sample spectrum points (interpolated with straight lines) and the Gaussian profile fitted to the average spectrum. This nominal value of this integral was used in the DFT procedure described in section 3.1.2. There was no electrical measurement to compare these results with.
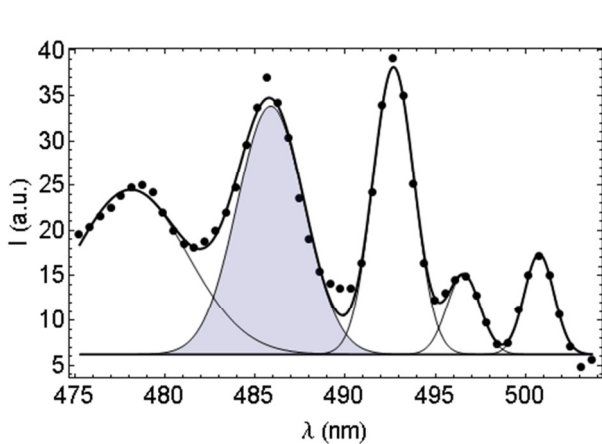
Figure 29: Gaussian fit on the H_β peak (shaded area). The sum of the Gaussians (thick line) was fitted to the averaged spectra (solid discs).
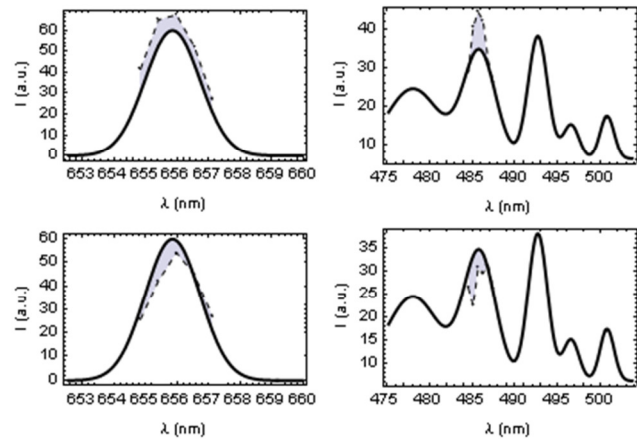
Figure 30: Examples of deviations (shaded area) from the H_α (left) and H_β (right) peaks. The dashed line denotes data from a single spectrum.

A series of OES spectra was taken at approximately 2 minutes after plasma ignition. The series had durations of 10 seconds and acquisition times of 1.1, 3, 5 and 100 ms. The signal-to-noise ratio of the 1.1 ms spectra was too low to be able to perform an analysis; the 3 and 5 ms spectra could be analysed and frequencies in the fluctuation of H_α, H_β, and the total spectrum were observed in the same range as found with the PMT (see Figure 27: triangles). In the H_α/H_β ratio there was no fluctuation observed. Complete results can be found in Appendix A and Appendix B.

3.2 TEMPERATURE CALIBRATION IN IRIS

In order to control the deposition temperature, it is important to know the relation between the (applied) heater temperature and the real substrate temperature. In this section, this substrate temperature calibration is described. In these experiments also the effect of a special stretch holder on a plastic substrate was investigated. As the plastic substrate bends under the influence of temperature, it has the tendency to hang down from the substrate holder. The stretch holder counteracts this by applying a stretching force on the substrate. The temperature was monitored at the centre and on the side of the substrate. Two different gas pressures were used: 0.16 mbar to resemble amorphous silicon deposition and 5 mbar to resemble microcrystalline silicon depositions.

With a constant argon pressure in a closed plasma chamber (without gas flow), the substrate temperature evolution during a series of 5-6 heater settings was recorded, so that the stabilized temperatures as well as the substrate temperature equilibration times could be measured. Also the effect of a plasma on the substrate

temperature was measured. The conditions as well as the observed equilibration times of a heater temperature increase of 20 °C are shown in Table 4.

Table 4: List of temperature calibrations together with the required substrate temperature equilibration time

holder	Pressure (mbar)	Equilibration time of 20 °C increase
normal	0.000	100-120 min.
normal	0.16	70 min.
normal	5.0	60 min.
stretch	0.16	80 min.
stretch	5.0	60 min.

The heating process was found to be dependent on the pressure: when the heater temperature was increased at 0.16 mbar, the substrate temperature increased asymptotically to a stable value, whereas at 5 mbar, the temperature overshot and then decreased to a stable value. An increase from room temperature to 100 °C took 120-150 minutes, depending on the gas pressure.

The relation between the applied heater temperature and the measured substrate temperature was fitted using linear regression (see Table 5). All fits were very good ($R^2 > 0.97$). The given uncertainties were estimated from the stability of the temperature.

Table 5: Relations between the substrate temperature and heater temperature in IRIS ($T_{subst} = a * T_{heat} + b$).

holder	substrate	0.000 mbar (°C)	0.16 mbar (°C)	5 mbar (°C)
normal	glass	$0.65\ T_{heat} - 8 \pm 3$	$0.66\ T_{heat} + 8 \pm 1$	$0.93\ T_{heat} + 0 \pm 1$
normal	polycarbonate side	$0.65\ T_{heat} - 5 \pm 3$	$0.64\ T_{heat} + 8 \pm 1$	$0.79\ T_{heat} + 7 \pm 1$
normal	polycarbonate middle	$0.63\ T_{heat} - 8 \pm 3$	$0.61\ T_{heat} + 7 \pm 1$	$0.74\ T_{heat} + 3 \pm 1$
stretch	glass middle		$0.66\ T_{heat} + 0 \pm 2$	$0.80\ T_{heat} + 4 \pm 2$
stretch	glass side		$0.66\ T_{heat} + 0 \pm 2$	$0.79\ T_{heat} + 3 \pm 2$
stretch	polycarbonate middle		$0.68\ T_{heat} + 0 \pm 2$	

During the measurements of the polycarbonate substrates in the normal sample holder, the sample hung 3-6 mm (increasing with temperature, partly reversibly) from the substrate holder. The stretch holder successfully counteracts this temperature induced deformation of the polycarbonate. Only after two full days of heating, the plastic started to hang down 1-2 mm (irreversibly) at the middle and correspondingly, the measured temperature became lower.

Also, several plasmas were investigated on both the normal and the stretch holder: a pure argon plasma, an amorphous silicon deposition plasma, and a microcrystalline silicon deposition plasma (see Table 3 on page 31 for the complete parameter set). With every plasma, there was a quick substrate heating of 1-3 °C observed, followed by a constant substrate heating of 1°C per 5-10 min.

3.3 SCATTERING EXPERIMENTS (LLS)

Several test measurements were done on dusty and dust-free regimes (see Table 3 on page 31). Two setups were tested. The short angle scattering setup suffered from too much stray light from the laser: a scattered signal could not be measured in this setup, because the laser background signal was too large.

The 90° setup was tested with plasmas under several conditions. The effectiveness of a collimator was tested, which was installed to reduce the stray light. Because the collimator lowered the laser intensity, these measurements were done at a higher PMT gain: $9.9 \cdot 10^5$ compared to $5.5 \cdot 10^5$. Full results are displayed in Table 6. The scattered intensity was calculated by subtracting the average of the plasma glow (without illumination) and the average of the total intensity (plasma with illumination). The error was calculated from the variance in both signals. Also the signal-to-noise ratio (SNR) is given. Finally, two background signals without a plasma were recorded, one with collimator and one without.

In some measurements the detector exhibited a constant drift. In these measurements, the average was taken over a short period of 1-3 seconds before and after the laser switch-off, so that the drift within this period was negligible compared to the signal noise.

Only in measurement numbers 60, 61, 67, 68, and 69 there was a significant scattering signal; all of these plasmas were in the dusty regime.

Table 6: Results of scattering measurements at 90° angle. SNR denotes the signal to noise ratio.

#	Plasma (Table 3)	Collimator	Gain	SiH$_4$:H$_2$ (sccm)	V$_{scat}$ (mV)			SNR	Comments
	no plasma	no	$5.5 \cdot 10^5$		3				multimeter
60	dusty	no	$5.5 \cdot 10^5$	30:30	54	±	10	5.4	
61	dusty	no	$5.5 \cdot 10^5$	30:30	68	±	10	6.8	
63	dust-free	no	$5.5 \cdot 10^5$	5:125	3	±	7	0.4	
64	dust-free	no	$5.5 \cdot 10^5$	25:125	4	±	4	1.0	
65	dust-free	no	$5.5 \cdot 10^5$	25:125	5	±	3	1.7	
72	no plasma	yes	$9.9 \cdot 10^5$		2.5	±	0.6		
67	dusty	yes	$9.9 \cdot 10^5$	30:30	146	±	18	8.1	drift
68	dusty	yes	$9.9 \cdot 10^5$	20:20	62	±	21	3.0	drift
69	dusty	yes	$9.9 \cdot 10^5$	15:15	888	±	241	3.7	drift
70	dusty	yes	$9.9 \cdot 10^5$	10:10	32	±	22	1.5	drift
73	dust-free	yes	$9.9 \cdot 10^5$	5:125	3	±	11	0.3	drift
74	dust-free	yes	$9.9 \cdot 10^5$	5:125	3	±	11	0.3	drift
75	dust-free	yes	$9.9 \cdot 10^5$	25:125	3	±	6	0.5	
76	dust-free	yes	$9.9 \cdot 10^5$	25:125	4	±	6	0.7	

Chapter 4 Conclusion and discussion

4.1 DUSTY PLASMA FLUCTUATION

A dusty SiH_4:H_2 plasma was found to exhibit a stable fluctuation of 10-50 Hz. The fluctuation was most pronounced in the overall optical emission and was also observed in the electric properties. No fluctuation of the electron temperature could be detected with the optical emission spectrometer due to its low signal to noise ratio. The frequency of the fluctuation showed trends with the variation of temperature and total gas flow: an increased temperature was observed to have a slowing effect on the fluctuation and an increased total gas flow rate resulted in an increase of the fluctuation frequency.

The plasmas were all in the γ' regime, and therefore the plasma dust is assumed to be in its last growth phase with diameters > 100 nm. The growth gas phase growth of dust particles occurs via a process similar to the layer deposition.

An increased temperature has multiple effects on a plasma, of which the most important one is that chemical reactions are faster. The thermal energies of the neutrals particles and ions increase. Because of the resulting increased ion flux, the dust charge is reduced (equation 26). Also, deposition rates are slightly higher at higher temperature [90]. An increase of flow rate results in a lower gas residence time and lower silane depletion. Also the neutral drag force increases.

Based on the observations and the literature study (section 1.3.4), it can be hypothesized that the fluctuation arises from a repeatedly forming and blowing away of a dust cloud, possibly via the often described void mechanism. An increase of flow rate could possibly increase the dust growth rate and thus the frequency of the fluctuation. However, when the silane depletion is reduced, the growth rate may not increase.

Next to the dust growth rate, the driving force of this generation instability is the ion drag. For the same dust size and charge, the ion scattering cross section decreases with ion temperature: ion drag becomes less when ion temperature increases (equations 24 and 30). This could be a reason for the slower fluctuation at higher temperature.

The timescale of the observed fluctuation is however entirely different from literature. Reported values of the generation instability are in the order of minutes (section 1.3.4), while the fluctuations measured here are 2 orders of magnitude faster. Another explanation for the observed fluctuation could be a void fluctuation, of which there is only very little knowledge in silane plasmas.

The dust acoustic wave is also a phenomenon in the right frequency range. For this phenomenon, the dust is considered as a medium for the fluctuation. Because the frequency is dependent on the characteristics of the medium (dust charge, size, and concentration), there should be a drift in the frequency, as dust is constantly growing. This was however not found in the experiments, so the fluctuation is probably not an acoustic wave.

4.2 TEMPERATURE CALIBRATION IN IRIS

The relation between heater and substrate temperature has been measured with different substrates, sample holders and plasma pressures. The substrate temperature was higher at higher pressures. If we compare these results with the rule of thumb 'substrate temperature = 5/7 times heater temperature', there is only little discrepancy in the 0.16 mbar regime (see Figure 31). In the 5 mbar regime however, the 5/7 rule is clearly underestimating the substrate temperature.
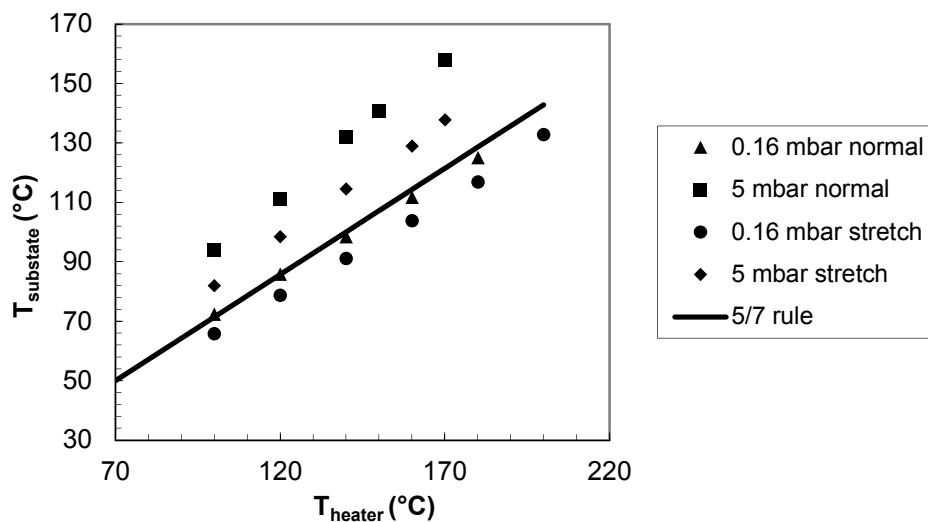
Figure 31: Comparison of the 5/7 rule to measured temperatures at the centre of a glass substrate in two holders and at two pressures

The overall temperature of substrates in the stretch holder is approximately 8 °C (0.16 mbar) or 10-20 °C (5 mbar) lower than substrates in a normal holder, probably due to the air between the sample and the stretch holder. The use of a stretch holder was found to be essential to homogeneously heat a plastic substrate.

From the temperature development, there are some other conclusions that are important for the control of the substrate temperature during thin film deposition:

- In vacuum, the temperature needs approximately 2.5 hours to stabilize for a heater temperature of 100 °C. An increase of 20 °C takes 100-120 minutes. This time is reduced by increasing the gas pressure: at a pressure of 5 mbar, an increase of 20 °C takes only 60 minutes.
- When a plasma is switched on (5-17.5 W input power), there is always a quick heating of 1-3 °C, followed by a constant substrate heating of 1°C per 5-10 min.

4.3 SCATTERING EXPERIMENTS (LLS)

Using the 90° scattering setup (see Figure 18 on page 35), a scattered signal was detected in several dusty plasmas. The scattering signals of the dust-free plasmas were not significantly larger than the background signal.

The background signal is the stray light: reflected laser light coming from diffuse reflections in the chamber windows, at the collimator or at the beam stop. As this stray light production is possibly also influenced by a plasma, in cannot be simply subtracted from the total signal intensity to obtain only the scattered light intensity. Therefore, the stray light should be reduced as much as possible.

One way to reduce this stray light is the use of the collimator, but because of the large drift in the measurements with collimator there can be no quantitative conclusions drawn and the advantage of the collimator was not proven. Supposedly, the collimator reduces the stray light scattering from the entrance window. On the other hand, the collimator reduces the laser intensity so that the detector has to be set at a higher gain and the detector signal to noise ratio increases.

4.4 OUTLOOK

In the near future, a new deposition chamber will be available. This chamber is especially designed for the plasma synthesis of silicon quantum dots (dust precursors in the range of 1-10 nm). As this is the fifth chamber of the multichamber deposition system ASTER, it can eventually be used for the production of quantum dot thin film solar cells.

The new chamber replaces the top electrode with a grid, through which dust particles are extracted from the plasma. The substrate is mounted behind the grid. A cooler is attached to the substrate and the grid is attached to the heater, so that a temperature gradient can establish a thermophoretic drift of the particles (see section 1.2.4). The pump is located behind the substrate, so that the gas drag force will also aid the particles in reaching the substrate. It has been proven that this type of chamber design is able to collect silicon quantum dots [91].

Scattering experiments can be done via three viewports behind the grid: a laser inlet window and detector windows at 0° and 90°. From the window at 0°, it is also possible to collect a 6° scattering signal. The optical emission of the plasma can be monitored and there are two viewports aligned to the substrate for using ellipsometry. See Figure 32 for a schematic of chamber 5.
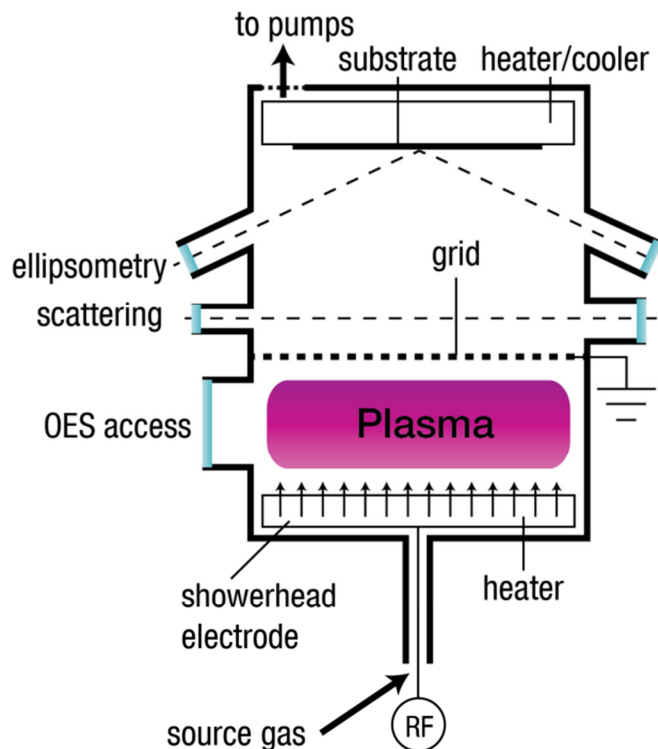

Figure 32: Schematic drawing of chamber 5

The plasma temperature and substrate temperature can be controlled independently to generate a temperature gradient. This temperature gradient generates an upwards thermophoretic drift of the dust particles. The electrode distance can be 10, 15 or 20 mm. The chamber will be used for the search of the ideal parameter set (temperatures, pressure, power, electrode distance, flow rates, hydrogen dilution) for the production of silicon quantum dots.

With this thesis, I hope to have made a contribution in the development of this chamber and eventually the production of a quantum dot based thin film solar cell. The temperature calibration method will help to control the temperature gradient in chamber 5 and the scattering setup will be used to detect the dust particles. The observed plasma fluctuation is interesting to implement as a fast diagnosis, possibly to indicate the stage of the dust growth or even quantify the dust growth rate.

4.5 ACKNOWLEDGMENT

Bibliography

[1] J. Wackerbauer and J. Lippelt, CESifo Forum 70–73 (2012).

[2] M. Edoff, Ambio **41**, 112–118 (2012).

[3] J. K. Rath, Applied Physics A **96**, 145–152 (2008).

[4] F. Dross, K. Baert, T. Bearda, J. Deckers, V. Depauw, O. el Daif, I. Gordon, A. Gougam, J. Govaerts, S. Granata, R. Labie, X. Loozen, R. Martini, A. Masolin, B. O'Sullivan, Y. Qiu, J. Vaes, D. van Gestel, J. van Hoeymissen, A. Vanleenhove, K. van Nieuwenhuysen, S. Venkatachalam, M. Meuris, and J. Poortmans, Progress in Photovoltaics: Research and Applications **20**, 770–784 (2012).

[5] A. M. Smith and S. Nie, Accounts of Chemical Research **43**, 190–200 (2010).

[6] P. K. Shukla and B. Eliasson, Reviews of Modern Physics **81**, 25–44 (2009).

[7] P. Roca i Cabarrocas, N. Chaâbane, A. V. Kharchenko, and S. Tchakarov, Plasma Physics and Controlled Fusion **46**, B235–B243 (2004).

[8] Y. M. Soro, A. Abramov, M. E. Gueunier-Farret, E. V. Johnson, C. Longeaud, P. Roca i Cabarrocas, and J. P. Kleider, Thin Solid Films **516**, 6888–6891 (2008).

[9] L. Boufendi, M. C. Jouanny, E. Kovačević, J. Berndt, and M. Mikikian, Journal of Physics D: Applied Physics **44**, 174035 (2011).

[10] J. P. Bœuf and C. Punset, in *Dusty Plasmas: Physics, Chemistry and Technological Impacts in Plasma Processing*, edited by A. Bouchoule (John Wiley & Sons Ltd., 1999).

[11] J. Perrin and C. Hollenstein, in *Dusty Plasmas: Physics, Chemistry and Technological Impacts in Plasma Processing*, edited by A. Bouchoule (John Wiley & Sons Ltd., 1999).

[12] L. Boufendi, W. W. Stoffels, and E. Stoffels, in *Dusty Plasmas: Physics, Chemistry and Technological Impacts in Plasma Processing*, edited by A. Bouchoule (John Wiley & Sons Ltd., 1999).

[13] A. Bouchoule, in *Dusty Plasmas: Physics, Chemistry and Technological Impacts in Plasma Processing*, edited by A. Bouchoule (John Wiley & Sons Ltd., 1999).

[14] V. E. Fortov, A. V. Ivlev, S. A. Khrapak, A. G. Khrapak, and G. E. Morfill, Physics Reports **421**, 1–103 (2005).

[15] K. Ostrikov, U. Cvelbar, and A. B. Murphy, Journal of Physics D: Applied Physics **44**, 174001 (2011).

[16] H. J. de Blank, *PLASMA PHYSICS Lecture Notes* (FOM-Institute for Plasma Physics Rijnhuizen, 2011).

[17] R. Remy, Optical Diagnostics of Dusty Plasmas, Eindhoven University of Technology, 2005.

[18] W. J. Goedheer, *Lecture Notes: Direct Current and Radio-Frequency Discharges* (FOM-Institute for Plasma Physics Rijnhuizen, 2011).

[19] M. N. van den Donker, B. Rech, F. Finger, L. Houben, W. M. M. Kessels, and M. C. M. van de Sanden, Progress in Photovoltaics: Research and Applications **15**, 291–301 (2007).

[20] D. Hrunski, W. Grählert, H. Beese, T. Kilper, A. Gordijn, and W. Appenzeller, Thin Solid Films **517**, 4188–4191 (2009).

[21] A. Verkerk, Plasma Deposition of Thin Film Silicon at Low Substrate Temperature and at High Growth Rate, Utrecht University, 2009.

[22] E. Amanatides, S. Stamou, and D. Mataras, Journal of Applied Physics **90**, 5786 (2001).

[23] J. Perrin, O. Leroy, and M. C. Bordage, Contributions to Plasma Physics **36**, 3–49 (1996).

[24] P. Roca i Cabarrocas, in *Physics and Technology of Amorphous-Crystalline Heterostructure Silicon Solar Cells*, edited by W. G. J. H. M. Sark, L. Korte, and F. Roca (Springer Berlin Heidelberg, 2011), pp. 131–160.

[25] A. A. Howling, B. Strahm, and C. Hollenstein, Thin Solid Films **517**, 6218–6224 (2009).

[26] A. Gallagher, A. A. Howling, and C. Hollenstein, Journal of Applied Physics **91**, 5571 (2002).

[27] K. de Bleecker, A. Bogaerts, R. Gijbels, and W. J. Goedheer, Physical Review E **69**, 1–16 (2004).

[28] A. Gallagher, Physical Review E **62**, 2690–706 (2000).

[29] C. Hollenstein, Plasma Physics and Controlled Fusion **42**, R93–104 (2000).

[30] C. Courteille, C. Hollenstein, J. Dorier, P. Gay, W. Schwarzenbach, A. A. Howling, E. Bertran, G. Viera, R. Martins, and A. Macarico, Journal of Applied Physics **80**, 2069 (1996).

[31] L. Boufendi, A. Bouchoule, and T. Hbid, Journal of Vacuum Science and Technology A **14**, 572–576 (1996).

[32] P. Belenguer, J. P. Blondeau, L. Boufendi, M. Toogood, A. Plain, A. Bouchoule, C. Laure, and J. P. Bœuf, Physical Review A **46**, 7923–33 (1992).

[33] A. Bouchoule, A. Plain, L. Boufendi, J. P. Blondeau, and C. Laure, Journal of Applied Physics **70**, 1991 (1991).

[34] J. de Koning, Observations on the Transition from a- to Y'-plasma Regime by the Use of Optical Emission Spectroscopy at Different Substrate Temperatures, Utrecht University, 2009.

[35] M. M. de Jong, J. de Koning, J. K. Rath, and R. E. I. Schropp, Physics of Plasmas **19**, 020703 (2012).

[36] S. A. Khrapak, S. Ratynskaia, A. Zobnin, A. Usachev, V. Yaroshenko, M. Thoma, M. Kretschmer, H. Höfner, G. E. Morfill, O. Petrov, and V. E. Fortov, Physical Review E **72**, 1–10 (2005).

[37] W. J. Goedheer, V. Land, and J. Venema, Contributions to Plasma Physics **49**, 199–214 (2009).

[38] J. Goree, G. E. Morfill, V. N. Tsytovich, and S. V. Vladimirov, Physical Review E **59**, 7055–67 (1999).

[39] J. Berndt, E. Kovačević, I. Stefanović, O. Stepanović, S. H. Hong, L. Boufendi, and J. Winter, Contributions to Plasma Physics **49**, 107–133 (2009).

[40] A. Piel and A. Melzer, Plasma Physics and Controlled Fusion **44**, R1–R26 (2002).

[41] G. Gozadinos, A. V. Ivlev, and J. P. Bœuf, New Journal of Physics **5**, 1–9 (2003).

[42] G. J. Nienhuis, W. J. Goedheer, E. A. G. Hamers, W. G. J. H. M. van Sark, and J. Bezemer, Journal of Applied Physics **82**, 2060 (1997).

[43] W. J. Goedheer and V. Land, Plasma Physics and Controlled Fusion **50**, 124022 (2008).

[44] A. D. Richards, B. E. Thompson, and H. H. Sawin, Applied Physics Letters **50**, 492 (1987).

[45] M. Cavarroc, M. Mikikian, G. Perrier, and L. Boufendi, Applied Physics Letters **89**, 013107 (2006).

[46] W. W. Stoffels, E. Stoffels, G. M. W. Kroesen, and F. J. de Hoog, Journal of Applied Physics **78**, 4867 (1995).

[47] L. Boufendi and A. Bouchoule, Plasma Sources Science and Technology **262**, (1994).

[48] G. Praburam and J. Goree, Physics of Plasmas **3**, 1212 (1996).

[49] D. Samsonov and J. Goree, Physical Review E **59**, 1047–1058 (1999).

[50] M. Cavarroc, M. Mikikian, Y. Tessier, and L. Boufendi, Physical Review Letters **100**, 3–6 (2008).

[51] E. V. Johnson, Y. Djeridane, A. Abramov, and P. Roca i Cabarrocas, Plasma Sources Science and Technology **17**, 035029 (2008).

[52] M. Mikikian and L. Boufendi, Physics of Plasmas **11**, 3733 (2004).

[53] M. Mikikian, L. Couëdel, M. Cavarroc, Y. Tessier, and L. Boufendi, New Journal of Physics **9**, 268 (2007).

[54] M. Cavarroc, M. Mikikian, Y. Tessier, and L. Boufendi, Physics of Plasmas **15**, 103704 (2008).

[55] M. Mikikian, M. Cavarroc, L. Couëdel, Y. Tessier, and L. Boufendi, Pure and Applied Chemistry **82**, 1273–1282 (2010).

[56] L. Boufendi, J. Gaudin, S. Huet, G. Viera, and M. Dudemaine, Applied Physics Letters **79**, 4301 (2001).

[57] G. Wattieaux, A. Mezeghrane, and L. Boufendi, Physics of Plasmas **18**, 093701 (2011).

[58] A. Mezeghrane, M. Jouanny, M. Cavarroc, M. Mikikian, O. Lamrous, and L. Boufendi, in *Proceedings of the 31st EPS Conference on Plasma Physics* (European Physical Society, London, 2004), p. 28G, O–1.09.

[59] S. Nunomura, I. Yoshida, and M. Kondo, Applied Physics Letters **94**, 071502 (2009).

[60] Y. Watanabe, Journal of Physics D: Applied Physics **39**, R329–R361 (2006).

[61] U. Fantz, Plasma Physics and Controlled Fusion **40**, 1035–1056 (1998).

[62] M. M. de Jong, On the Influence of Substrate Temperature on Plasma Characteristics, Utrecht University, 2009.

[63] M. Takai, T. Nishimoto, M. Kondo, and A. Matsuda, Thin Solid Films **390**, 83–87 (2001).

[64] J. K. Rath, R. H. J. Franken, A. Gordijn, R. E. I. Schropp, and W. J. Goedheer, Journal of Non-Crystalline Solids **338-340**, 56–60 (2004).

[65] A. A. Howling, B. Strahm, P. Colsters, L. Sansonnens, and C. Hollenstein, Plasma Sources Science and Technology **16**, 679–696 (2007).

[66] L. Feitknecht, J. Meier, P. Torres, J. Zurcher, and A. Shah, Solar Energy Materials and Solar Cells **74**, 539 (2002).

[67] J. K. Rath, A. D. Verkerk, R. E. I. Schropp, B. Boussadkat, and W. J. Goedheer, Journal of Non-Crystalline Solids **358**, 1995–1999 (2012).

[68] G. S. Selwyn, J. Singh, and R. S. Bennett, Journal of Vacuum Science and Technology A **7**, 2758–2765 (1989).

[69] D. Mataras, S. Cavadias, and D. Rapakoulias, Journal of Applied Physics **66**, 119–24 (1989).

[70] A. Kono, N. Koike, K. Okuda, and T. Goto, Japanese Journal of Applied Physics **32**, 543–6 (1993).

[71] M. Hertl, J. Jolly, and G. Baravian, Journal of Applied Physics **92**, 710 (2002).

[72] L. Sansonnens, A. A. Howling, and C. Hollenstein, Plasma Sources Science and Technology **7**, 114–118 (1998).

[73] B. Strahm, A. A. Howling, L. Sansonnens, and C. Hollenstein, Plasma Sources Science and Technology **16**, 80–89 (2007).

[74] G. Parascandolo, R. Bartlome, G. Bugnon, T. Söderström, B. Strahm, A. Feltrin, and C. Ballif, Applied Physics Letters **96**, 233508 (2010).

[75] W. M. M. Kessels, K. Nadir, and M. C. M. van de Sanden, Journal of Applied Physics **99**, 076110 (2006).

[76] L. Boufendi, J. Hermann, A. Bouchoule, and B. Dubreuil, Journal of Applied Physics **76**, 148–53 (1994).

[77] F. R. A. Onofri, M. Wozniak, and S. Barbosa, Contributions to Plasma Physics **51**, 228–236 (2011).

[78] E. A. G. Hamers, W. G. J. H. M. van Sark, J. Bezemer, W. J. Goedheer, and W. F. van der Weg, International Journal of Mass Spectrometry and Ion Processes **173**, 91–98 (1998).

[79] A. Imhof, in *Soft Condensed Matter* (Universiteit Utrecht, 2012), pp. 55–82.

[80] S. Nunomura, M. Kita, K. Koga, M. Shiratani, and Y. Watanabe, Journal of Applied Physics **99**, 083302 (2006).

[81] A. R. Forouhi and I. Bloomer, Physical Review B **34**, 7018 (1986).

[82] V. Suendo, Low Temperature Plasma Synthesis of Silicon Nanocrystals for Photonic Applications, Ecole Polytechnique, 2005.

[83] J. Pender, M. Buie, T. Vincent, J. Holloway, M. Elta, and M. L. Brake, Journal of Applied Physics **74**, 3590 (1993).

[84] M. Shiratani, T. Fukuzawa, and Y. Watanabe, Japanese Journal of Applied Physics **38**, 4542–4549 (1999).

[85] F. Huang, M. Ye, and L. Wang, Science in China Series G: Physics, Mechanics and Astronomy **49**, 588–596 (2006).

[86] B. Strahm and C. Hollenstein, Journal of Applied Physics **107**, 023302 (2010).

[87] E. A. G. Hamers, Plasma Deposition of Hydrogenated Amorphous Silicon, Utrecht University, 1998.

[88] NIST, ITS-90 Thermocouple Database (1990).

[89] D. W. Jordan and P. Smith, *Mathematical Techniques*, 4th ed. (Oxford university press, 2008).

[90] A. D. Verkerk, M. M. de Jong, J. K. Rath, M. Brinza, R. E. I. Schropp, W. J. Goedheer, V. V. Krzhizhanovskaya, Y. E. Gorbachev, K. E. Orlov, E. M. Khilkevitch, and A. S. Smirnov, Materials Science and Engineering: B **159-160**, 53–56 (2009).

[91] M. Shiratani, K. Koga, S. Ando, T. Inoue, Y. Watanabe, S. Nunomura, and M. Kondo, Surface and Coatings Technology **201**, 5468–71 (2007).

Appendix A   **Results of emission measurements**

#	date	T (°C)	Q (sccm)	Setup	Frequency (Hz)
13	17 Nov '11	175	105.0	PMT A bulk H_α	29.4 ± 0.10
14	17 Nov '11	175	105.0	PMT A sheath H_α	28.7 ± 0.04
15	17 Nov '11	175	105.0	PMT A sheath SiH	28.8 ± 0.02
16	17 Nov '11	175	105.0	PMT A bulk SiH	30.0 ± 0.08
17	17 Nov '11	189	105.0	PMT A bulk SiH	26.9 ± 0.05
18	17 Nov '11	197	105.0	PMT A sheath SiH	25.2 ± 0.10
19	17 Nov '11	194	105.0	PMT A sheath H_α	26.0 ± 0.09
20	17 Nov '11	199	105.0	PMT A bulk H_α	26.1 ± 0.10
21	17 Nov '11	205	105.0	PMT A bulk H_α	28 to 26
22	17 Nov '11	214	105.0	PMT A sheath H_α	25.1 ± 0.14
23	17 Nov '11	222	105.0	PMT A sheath SiH	24.2 ± 0.10
24	17 Nov '11	220	105.0	PMT A bulk SiH	24.1 ± 0.05
27	8 Dec '11	180	60.0	PMT A bulk H_α	14.0 ± 0.03
28	8 Dec '11	180	80.0	PMT A bulk H_α	21.3 ± 0.04
29	8 Dec '11	180	105.0	PMT A bulk H_α	37.5 ± 0.02
30	8 Dec '11	180	120.0	PMT A bulk H_α	42.8 ± 0.03
31	8 Dec '11	180	60.0	PMT A bulk SiH	13.7 ± 0.03
32	8 Dec '11	180	80.0	PMT A bulk SiH	29.1 ± 0.07
33	8 Dec '11	180	105.0	PMT A bulk SiH	38.9 ± 0.4
34	8 Dec '11	180	120.0	PMT A bulk SiH	42.0 ± 0.12
78	27 Mar '12	180	126.0	PMT B H_α	34.1 ± 0.09
79	27 Mar '12	180	115.5.	PMT B H_α	30.8 ± 0.07
80	27 Mar '12	180	105.0	PMT B H_α	28.8 ± 0.08
81	27 Mar '12	180	94.5	PMT B H_α	17.0 ± 0.09
82	27 Mar '12	180	84.0	PMT B H_α	17.4 ± 0.16
83	27 Mar '12	180	73.5	PMT B H_α	21.4 ± 0.01
84	27 Mar '12	180	63.0	PMT B H_α	6.0 ± 0.04
85	27 Mar '12	180	52.5	PMT B H_α	none
86	27 Mar '12	180	42.0	PMT B H_α	none
87	27 Mar '12	180	31.5	PMT B H_α	none
88	27 Mar '12	180	21.0	PMT B H_α	none
89	27 Mar '12	180	12.6	PMT B H_α	none
90-93	2 Apr '12	180	105.0	OES	31.9
94-97	2 Apr '12	180	84.0	OES	27.2
99-100	20 Apr '12	180	63.0	OES	13.8
102-105	20 Apr '12	180	42.0	OES	none

Appendix B   Results of OES measurements

Values above the graphs are the frequencies of found peaks. The vertical axis was scaled automatically to the noise level of the DFT.